CO₂ sublimation in Martian gullies: laboratory experiments at varied slope angle and regolith grain sizes

MATTHEW E. SYLVEST[1,2]*, JOHN C. DIXON[1], SUSAN J. CONWAY[2,3], MANISH R. PATEL[2,4], JIM N. McELWAINE[5,6], AXEL HAGERMANN[2] & ADAM BARNES[7]

[1]*Arkansas Centre for Space and Planetary Sciences, University of Arkansas, Fayetteville, Arkansas, USA*

[2]*School of Physical Sciences, Open University, Milton Keynes, UK*

[3]*CNRS UMR 6112, Laboratoire de Planétologie et Géodynamique, Université de Nantes, Nantes, France*

[4]*Space Science and Technology Department, STFC Rutherford Appleton Laboratory, Oxfordshire, UK*

[5]*Department of Earth Sciences, Durham University, Durham, UK*

[6]*Planetary Science Institute, Tucson, Arizona, USA*

[7]*Center for Advanced Spatial Technologies, University of Arkansas, Fayetteville, Arkansas, USA*

*Correspondence: Matthew.Sylvest@open.ac.uk

Abstract: Martian gullies were initially hypothesized to be carved by liquid water, due to their resemblance to gullies on Earth. Recent observations have highlighted significant sediment transport events occurring in Martian gullies at times and places where CO_2 ice should be actively sublimating. Here we explore the role of CO_2 sublimation in mobilizing sediment through laboratory simulation. In our previous experimental work, we reported the first observations of sediment slope movement triggered by the sublimation of CO_2 frost. We used a Mars regolith simulant near the angle of repose. The current study extends our previous work by including two additional substrates, fine and coarse sand, and by testing slope angles down to 10°. We find that the Mars regolith simulant is active down to 17°, the fine sand is active only near the angle of repose and the coarse sand shows negligible movement. Using an analytical model, we show that under Martian gravity motion should be possible at even lower slope angles. We conclude that these mass-wasting processes could be involved in shaping Martian gullies at the present day and intriguingly the newly reported CO_2-creep process could provide an alternative explanation for putative solifluction lobes on Mars.

Supplementary material: Video clips depicting sediment transport types are available at https://doi.org/10.6084/m9.figshare.5208847

When initially observed by the Mars Global Surveyor (Fig. 1), Martian gullies were reasoned to have been formed by flowing water (Malin & Edgett 2000). With the observation of active modification and extension of gullies (Dundas *et al.* 2012), the apparent lack of liquid water under current Martian surface conditions leads to increased interest in alternative formative mechanisms. CO_2 is abundant on Mars, both as a gas (accounting for *c.* 95% of the atmosphere; Bargery *et al.* 2011) and as solid ice at the surface. Although concentrated in seasonal polar ice caps (Hess *et al.* 1979), CO_2 ice has been

detected on the surface at latitudes down to 32.3° S (Vincendon 2015). Like Earth, the climate on Mars is seasonal, owing to the tilt of its axis of rotation relative to its orbital plane (25.2° v. 23.4° for Earth) driving winter expansion and summer retreat of the seasonal ice caps as the ice sublimates into the atmosphere (Hess *et al.* 1979).

Recent studies suggest that seasonal freezing and sublimation of CO_2 ice could be responsible for present-day gully activity on Mars (Diniega *et al.* 2010; Cedillo-Flores *et al.* 2011; Hansen *et al.* 2011; Dundas *et al.* 2012). These observations
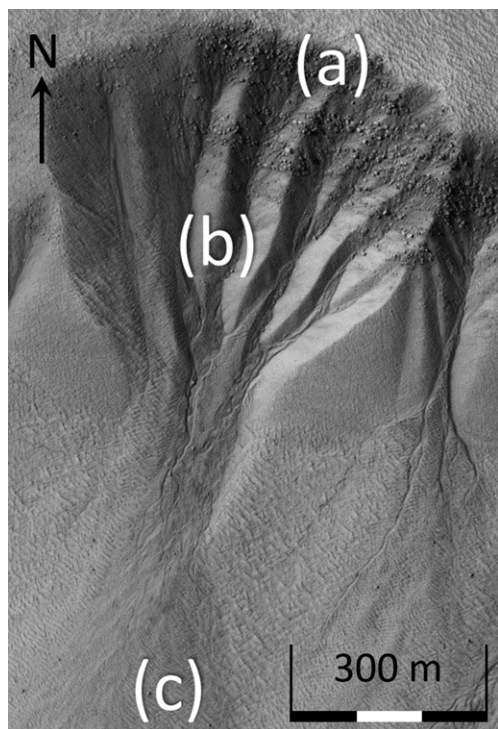
Fig. 1. A HiRISE gully monitoring image of a series of typical Mars gullies with source alcoves converging downslope (**a**) into a transport channel (**b**), which opens onto extensive depositional fans (**c**). Image: ESP_048424_1105_red – NASA/JPL/University of Arizona.

associate the timing of morphological changes with the seasonal CO_2 cycle (Reiss & Jaumann 2003; Dundas *et al.* 2010, 2012, 2014; Reiss *et al.* 2010; McEwen *et al.* 2011; Raack *et al.* 2015; Vincendon 2015; Pasquon *et al.* 2016) while experimental simulations (Diniega *et al.* 2013; Sylvest *et al.* 2016; McKeown *et al.* 2017) and numerical simulations (Cedillo-Flores *et al.* 2011; Pilorget & Forget 2016) demonstrate the efficacy of CO_2 slope mobilization models.

This work explores the ability of seasonal CO_2 frost to trigger slope failures of unconsolidated regolith. Previous experiments by Sylvest *et al.* (2016) established the ability of CO_2 frost to trigger mass wasting on slopes under Martian atmospheric conditions. Those experiments, however, were all conducted on slopes of JSC Mars-1 regolith simulant at approximately the angle of repose. This steep slope angle was chosen as it was the most likely to produce observable initial disruptions in a relatively short period of time. Yet clearly, Martian gullies and other mass wasting forms on Mars occur over a range

of slope angles: for instance, gullies commonly occur on slopes ranging from 10° to 30° (Dickson *et al.* 2007; Conway *et al.* 2015). JSC Mars-1 is a fine-grained volcanic tephra ranging in size from 13 μm to 1 mm (Allen *et al.* 1998), yet on Mars there is an exceedingly wide range of grain size distributions to be found in the soils at the planet's surface, ranging from very fine sand to coarse sand, together with a fine dust component (McGlynn *et al.* 2011).

While there have been Mars-focused experimental studies undertaken on the role of slope on the morphological characteristics of slope disturbances under both Earth surface conditions (Coleman *et al.* 2009; Jouannic *et al.* 2015) and Martian conditions (Jouannic *et al.* 2015), no studies have systematically examined the role of slope over a range of angles known to support a variety of mass wasting forms, including gullies. Similarly, a few experimental studies have systematically investigated the role of grain size in influencing the movement of debris under Martian atmospheric conditions (Conway *et al.* 2011a). These studies, however, examined water flow rather than CO_2 frost sublimation.

The experiments reported in this paper explore the influence of sediment grain size and initial slope angle on the ability of sublimating CO_2 ice to trigger mass wasting under Martian conditions.

Methods

A total of 28 experimental runs, including two control runs, were performed in the Mars Simulation Chamber (MSC) at the Open University, Milton Keynes, UK (Fig. 2). This cylindrical vacuum chamber, 2 m long by 1 m in diameter, is capable of replicating Martian atmospheric temperatures and pressures. Three regolith simulants were used at several initial slope angles, summarized in Table 1.

Each simulant was first tested at the angle of repose (AOR), as this is the least stable initial slope angle possible, and therefore the most likely condition to support the triggering of mass wasting (Sylvest *et al.* 2016). Subsequent angles were then selected based on the observed results of each previous run for that simulant.

The apparatus and procedures used for this work were adapted from Sylvest *et al.* (2016). Each run required preparation of the initial slope, preparation of the chamber atmosphere, cooling of the slope, condensation of CO_2 frost and, finally, sublimation of the frost. The only modifications to the methods of Sylvest *et al.* (2016) were in the initial slope preparation. Below, we present the slope preparation procedure and briefly summarize the remaining procedures.

Slope preparation started with vacuum drying the regolith, followed by stirring to disaggregate any

Fig. 2. The Large Mars Planetary Environmental Simulations Chamber (centre), vacuum pump (bottom), liquid nitrogen supply (left) and CO$_2$ gas cooler (front left of centre).

clumps and to help maintain a consistent initial bulk density and grain sorting between runs (Sylvest *et al.* 2016). The initial slope angle was then prepared by raking the regolith into a smooth, uniform slope with a plastic spatula. The angle was checked with a spirit-level protractor at three locations across the crest slope zone (Fig. 4a). The nominal slope angle for the run (Table 1) was based on the crest slope zone. The same *c.* 30 cm long, 20 cm wide, 12 cm deep test section from Sylvest *et al.* (2016) was reused.

The MSC was initially evacuated and purged with N$_2$ to remove moisture and provide a non-condensing atmosphere for the regolith cooling procedure. The regolith was cooled by flowing liquid N$_2$ through the test section coils (Sylvest *et al.* 2016) until the maximum near-surface temperature was cold enough to ensure condensation (−120°C, Table A1) of the relatively warm CO$_2$ gas (*c.* −20°C) at reduced chamber pressure (*c.* 350 mbar, Table A1). The chamber pressure typically reduced to *c.* 160 mbar during the cooling procedure, without pumping.

During the condensation procedure, CO$_2$ gas, cooled in a heat exchanger by the exhausted liquid N$_2$ (Fig. 2), was gently diffused (Figs 3d & 4b) over the regolith slope with the test section lid closed (Figs 3f & 4b). By keeping the lid closed, the CO$_2$

Table 1. *Regolith simulants and initial slope angles*

Regolith simulant	Bulk density (g cm^{-3})	Porosity	Permeability (m^2)	Particle density (g cm^{-3})	Initial slope angles					
					10°	15°	17.5°	20°	25°	AOR (*c.* 30°)
*JSC Mars-1	0.871	0.637	2.34 × 10^{-12}	2.40	X	X	X	X	X	X
†Fine sand	1.68	0.373	1.51 × 10^{-10}	2.68	X	X	n.d.	X	X	X
†Coarse sand	1.7	0.365	5.99 × 10^{-10}	2.68	n.d.	n.d.	n.d.	n.d.	n.d.	X

*Sizemore & Mellon (2008).
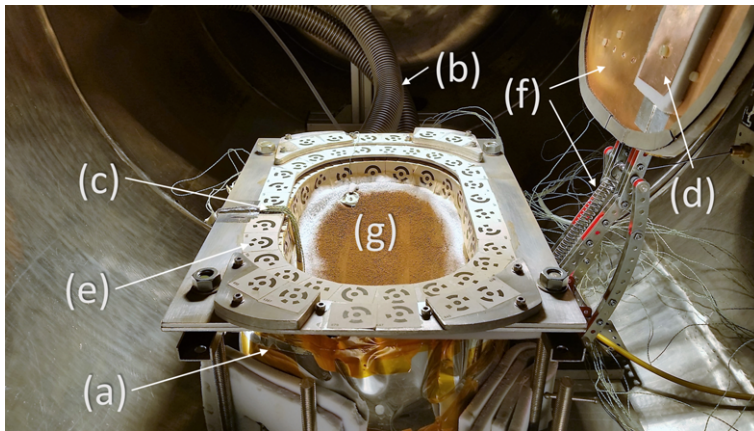†Laboratory analysis from Conway *et al.* (2011*b*).
n.d., No data.

Fig. 3. A view of an experiment inside the Mars chamber, at the start of sublimation. (**a**) The copper-coil regolith cooling box, externally insulated with open-celled foam and Mylar. (**b**) Insulated liquid nitrogen supply and exhaust lines. (**c**) Thermocouple wires were routed along the box wall and bottom to reach the thermocouple trees (Fig. 4a) with minimal influence on the regolith. (**d**) The CO_2 inlet diffuser reduced the likelihood of disturbing the regolith surface during the condensation procedure. (**e**) Coded photogrammetric targets were affixed at multiple heights and orientations. (**f**) The box lid and actuator were used to isolate the regolith from thermal radiation during the cooling and condensation procedures, exposing the surface only for the sublimation procedure. (**g**) The regolith simulant for this run was JSC Mars-1. Parallel, long-slope marks were left from the protractor used during slope preparation.

frost was prevented from forming on the horizontal photogrammetric markers which were glued to aluminium mounting surfaces.

The chamber pressure was pumped down to a representative Mars surface pressure of 5–7 mbar (Table A1; Hess *et al.* 1980) during the final 20 min of the frost condensation procedure.

Finally, the test section lid was opened and the frosted regolith surface exposed to a simulated insolation of *c.* 350 W m^{-2} maximum heat flux (Table A1) while recording the surface with stereo videography for photogrammetric analyses (Fig. 4b; Sylvest *et al.* 2016).

For each run, initial and terminal slope angles were recorded manually. Temperatures were recorded continuously at several depths in two locations along the centreline of the slope (Fig. 4a) and are summarized in Table A2. Pressure within the MSC was logged manually throughout each run (Sylvest *et al.* 2016).

Regolith simulants

JSC Mars-1, fine sand and coarse sand were selected as regolith simulants to identify possible controls on slope stability related to CO_2 ice sublimation, primarily owing to grain size distributions, but also to regolith composition. JSC Mars-1, a volcanic tephra, is the finest grained of the three simulants, with a broad grain size distribution from 13 μm to 1 mm (Allen *et al.* 1998). The fine sand regolith simulant is a well-sorted, dry silica sand with particle sizes

between 100 and 300 μm. Based on sieve analysis, the coarse sand is poorly sorted, with particle sizes between 3 mm and 125 μm. The hydraulic properties pertinent to slope stability and fluid dynamic analyses of all three simulants are listed in Table 1. Grain size distributions are presented in Appendix A (Figs A1–A3).

Photogrammetric methods

The photogrammetric methods used for this study are an extension of those developed by Sylvest *et al.* (2016). As in that work, two identical Sony HDR-CX330 camcorders were used to simultaneously and stereoscopically record slope surface activity in high definition (Fig. 4b). Coded photogrammetric targets were precisely located at multiple levels and orientations on the cooling box (Fig. 3e). These targets provide external control for all aspects of the photogrammetric project, establishing a common three-dimensional frame of reference (and therefore scale) for all aspects of the photogrammetric models. The video recordings were then processed (Fig. 5) to produce quantitative data. Each pair of videos was synchronized, and then image pairs were captured at 10 min time steps using Sony Vegas Pro 13 (Sylvest *et al.* 2016). The image pairs were imported into Agisoft PhotoScan Pro 1.2.6 and a series of digital elevation models (DEMs) was generated, one DEM for each time step.

There are two primary steps involved with the DEM production. The first step involves applying a
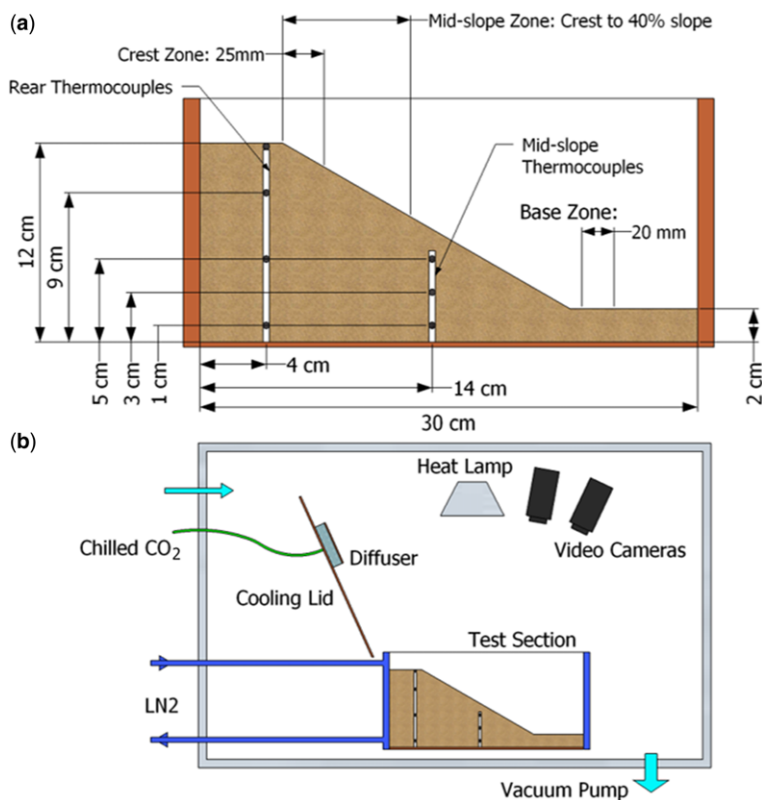
Fig. 4. Mars Chamber schematics. (**a**) Cut-away of copper cooling box with nominal dimensions. The two thermocouple trees were positioned along the centreline of the box. In all but the first six runs, an additional thermocouple (not shown) was positioned near the surface at the toe of the slope, *c.* 2 cm from the box wall. The 'Crest', 'Mid-slope' and 'Base' slope zones are also indicated. (**b**) Interior of the Mars Chamber, illustrating the relative positions of the cooling box, video cameras and heat lamp. The cooling lid remained closed throughout the cooling and condensation procedures, and then opened for sublimation.

photogrammetric bundle adjustment to determine interior (i.e. focal length, principal point and lens distortions) and exterior (i.e. camera positions and orientations) camera parameters. This step will henceforth be referred to as image alignment. The second step is the extraction of a dense 3D surface using multi-view stereo techniques. It is important to note that the two primary camera positions provided full stereoscopic coverage for all coded targets and the experimental surface. However, typically more than two camera positions are necessary to photogrammetrically model the above-mentioned camera parameters. Therefore, in order to improve the overall geometry of the photogrammetric block, the two primary camera positions were supplemented with images recorded from various positions around the box before the start of cooling, thus providing a much larger, virtual set of cameras. The use of these additional camera positions and coded targets with known coordinates (i.e. control points)

provides a strong photogrammetric network with a reprojection error of less than one pixel.

During the image alignment step in PhotoScan, the regolith surface was masked out of each image and a sparse set of 3D tie points was generated using the 'Align Photos' tool. This process involves automatically detecting and matching corresponding features across overlapping images. The coded targets were also detected by PhotoScan and the known coordinates for these targets were provided. In some instances, PhotoScan incorrectly measured and/or labelled the coded targets and manual adjustments of the marker(s) were necessary (Fig. 5). After necessary marker corrections were made, the photogrammetric block was then optimized using the bundle adjustment. Next, a dense 3D surface was extracted from the primary image pair and the resulting surface geometry compared with the known dimensions of the box. If the model was unsatisfactory, the marker locations for each coded target were
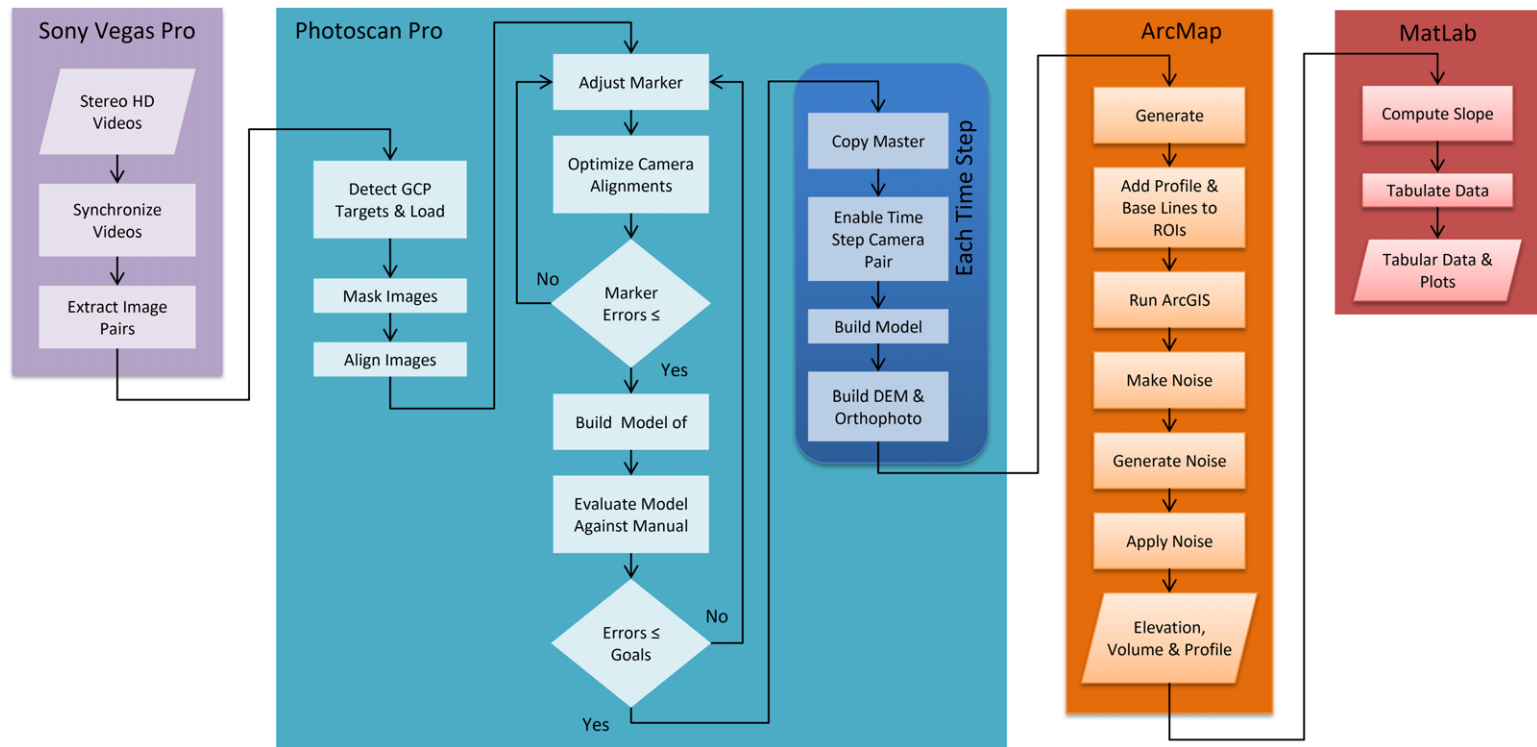
Fig. 5. Photogrammetric pipeline. The procedure for extracting data from the stereo video recordings made use of three principal software packages. Sony Vegas Pro was used to synchronize and extract coordinated image pairs for each DEM. Photoscan Pro was used to develop the DEMs based on the image pairs and physically measured target locations. Additionally, known hardware dimensions and measured slope angles were used to evaluate the accuracy of each DEM. The DEMs were then processed with ArcMap to derive volumetric and angular changes between DEMs. Finally, MatLab was used to compute slope angles and prepare the data for interpretation and presentation.

manually refined in each image, and additional tie points could be added, based on the nature of the error. This process was repeated (Fig. 5) until consecutive results were unimproved.

After the image alignment procedure, a sequence of DEMs (e.g. Fig. 7b) at 1 mm/pixel resolution were produced (one for each pair of images), now masking all but the slope inside the box. Likewise, a sequence of corresponding orthophotos at c. 0.29 mm/ pixel (e.g. Fig. 7a) was produced. Rasters of the elevation differences between consecutive DEMs were calculated in ESRI ArcMap 10.3.1. The region of interest (ROI) for each sequence of DEMs was determined within ArcMap by combining all the orthophotos for the sequence into a single shape that encapsulates the full extents of all the DEMs.

The difference rasters were multiplied by the DEM cell size (1 × 1 mm) to determine the erosional and depositional volumes. The volume of frost condensed on each slope was taken as the net deposition between the pre-condensation time step and the start of the sublimation procedure. The DEMs were also used to generate long profiles, used to characterize slope angles. The long profiles were generated by constructing a ROI 4 cm wide along the length of the slope in each DEM, and averaging the heights every 4 mm along the slope. Linear least squares fits were applied to the binned data in the three zones, crest, mid and base, as indicated in Figure 4a.

In order to reduce systematic volumetric noise artefacts in the DEMs, a new filtering procedure was added to the original methodology of Sylvest et al. (2016). For each difference raster, representing the change elevations between two DEMs, ArcMap was used to find contiguous volumes of transported regolith. A mask was generated by eliminating all but those volumes with areal extents below an interactively determined threshold, typically around 40 cm^2. This volume filter mask was then applied to the original difference raster, thereby reducing the photogrammetric noise. The filtered results were then imported into MathWorks Matlab 2016a in order to calculate slope angles and changes of angle for each slope zone (Fig. 4b), as well as to tabulate and plot the data.

Control runs and error estimation

The list of potential sources of error in the photogrammetric results, and the difficulty in assessing the contribution of any one of these sources, renders a direct error computation impractical (Raack et al. 2017). In order to quantify the 'uncertainty envelope' on a case-by-case basis, we evaluated differences in DEMs for slope regions known (by observation) to be devoid of sediment movement (as detailed later in this section). Table A3 lists the potential sources of error we have identified with our methods.

Control runs were performed for JSC Mars-1 and fine sand. A control run was deemed unnecessary for coarse sand, given the lack of substantial sediment movement observed for those runs. No sediment transport was observed for either of the two control runs. The control runs were configured at an initial slope at the static AOR and followed the same protocol used for the data runs, except that no CO$_2$ was introduced into the chamber during the condensation phase of the experiment. (See Sylvest et al. 2016 for full details of the experimental procedures.)

We did not use the control runs to calculate the errors on volumes and slopes, as potential sources of error, such as those listed in Table 4, varied between runs. For example, dense accumulations of surface frost are particularly difficult to model under the harsh lighting of the simulated insolation. The direction and intensity of the lamp (Fig. 4b) tends to eliminate shadows necessary to detect the surface features, which in turn are required for the dense surface reconstruction. Also, the high albedo of the frost tends to oversaturate the camera sensor, further obscuring features on the surface of the frost. Hence, during runs with more extensive surface frost coverage, noise in the surface model was more significant than for other runs. To allow for these variabilities, we developed a method to estimate errors using the difference DEMs for each run individually. Specifically, for each run, a small ROI (4.67 cm^2) was located on a portion of the slope where no movement was visually observed. The vertical noise was estimated as the mean change of elevation over the ROI, when comparing the first and last DEMs of the run. As in Sylvest et al. (2016), horizontal coordinate error estimates were based on the RMS errors for the coded target locations reported by PhotoScan, which were c. 1.0 mm for all runs. The equivalent vertical error for each of the runs, derived from the noise estimation procedure described above, ranged from 0.43 to 2.29 mm (Appendix A, Table A5). As in Sylvest et al. (2016), the standard accumulation of errors formulae were applied to these numbers in order to provide error estimates for each measured result.

Results

In the following sections, we describe the shared features of all the experiments, including how these volumes of sediment were transported, their magnitudes and the observed changes in slope angle. Then, we discuss the results for each sediment type separately.

Quantitative results

Substantial volumes of sediment were transported for JSC Mars-1 at initial slope angles from 17.5° to the AOR (*c.* 30°) and for fine sand at the AOR (Table 2). Between 1% and 14% of the total sediment volume was transported at initial target slope angles between 17.5° and the static angle of repose (AOR *c.* 30°) for JSC Mars-1, while between 2% and 4% of the total sediment volume was transported at the AOR for fine sand, also *c.* 30° (Table 3). Measured volumes of observed sediment transport for coarse sand at the AOR were less than 1% of the slope volume, well below the noise level of the photogrammetric results of 1.3% of the total slope volume (run 26, Table 5). Owing to the lack of sediment transport for coarse sand at the AOR, no additional runs were conducted with gentler slopes (Table 2). The maximum volumes eroded and deposited for all runs were 10.9% and 14.0% of the total slope volume, respectively, both recorded for run 24 (Table 3). These volumes correspond to maximum changes in slope elevation 47 mm for erosion, and 42 mm for deposition (Table 3).

Initial and final slope angles for each slope zone (Fig. 4a) are reported in Table 3, along with their associated angular changes. For the majority of the 25 runs with photogrammetric data, the angles of the crest and mid-slope zones changed very little (−1.1 ± 0.4° and −1.3 ± 0.4° on average, respectively). Only two JSC Mars-1 runs (runs 20 and 24, Table 3) underwent crest slope angle reductions greater than 8°. Base slope zone angles reduced by 3.6 ± 0.3° on average. No statistically significant correlations were found between initial slope angle or initial frost volume with elevation, volumetric or angular changes (see Appendix A for correlation results).

Sediment transport types

Sediment transport was observed in 20 of the 26 experimental runs conducted. Four types of sediment transport were identified in various combinations for each of the runs in Table 4. The most readily observed type is discrete granular flow. These flows are up to several centimetres wide, and can extend as far as the base of the slope, where they form depositional fans and lobes. They generally display well-defined areal extents, and occur on all but the gentlest slopes. When occurring concurrently, discrete flows frequently coalesce into larger composite flows, occasionally encompassing the full breadth and majority of the length of the slope. These flows can initiate on slope regions with no topographically induced instabilities, but only initiate on regions devoid of visible surface frost. Discrete granular flows were present in 19 of the 20 runs in which sediment transport was observed and recorded.

Second, in terms of volume transport, creep movements are more difficult to observe, generally requiring accelerated video playback to see their subtler movements. However, the areal extents of some creep movements were large enough to suggest substantial sediment transport volumes. Fourteen of the 26 runs were affected by creep (Table 4). Creep was not confined to any particular slope region; however, it was frequently present at the boundaries of retreating surface ice accumulations. These movements presented as narrow (<1 cm wide) bands of sediment, adjacent to and following the trailing edge of the retreating ice.

Sixteen of the 26 runs displayed obvious signs of gas entrainment of regolith particles. Although a common phenomenon, entrainment did not appear to be an effective sediment transport process on its own. Entrainment was most obvious at the toe of the slope, where sediment was deposited over surface frost. In these instances, the dusty surface gave the impression of boiling, owing to the vigorous sublimation of the shallowly buried frost. Evidence of escaping gas was also frequently observed where the thermocouple stations came close to, or in some cases became exposed at, the slope surface. These circular areas of activity were typically smaller and less active than the active areas at the slope base. For runs

Table 2. *Summary of regolith movement v. initial slope angle*

	10°	15°	17.5°	20°	25°	AOR (*c.* 30°)
JSC Mars-1	o	o	✓	✓	n.d.	✓
Fine sand	✓	o	n.d.	o	o	✓
Coarse sand	n.d.	n.d.	n.d.	n.d.	n.d.	✓

'✓', Substantial slope movement observed.
'o', No substantial slope movement observed.
n.d., No data for this initial slope angle.
Angles are initial target slope angles. Photogrammetrically measured values are presented in Table 3.
AOR, Static angle of repose.

with JSC Mars-1 at initial slope angles less than the angle of repose, fine dust deposits on the upslope box boundaries suggest that dust particles were entrained in the flow of CO_2 gas escaping from under the regolith along the warming box edge.

The fourth sediment transport type was the rolling and tumbling of individual, isolated grains; henceforth simply referred to as tumbling. Although tumbling grains of frost were common for many of the runs, they had no apparent effect on the underlying regolith; nor were they observed to trigger other modes of transport. Tumbling regolith particles were only observed in the two coarse sand runs (Table 4). This may be due in part to the much smaller, more uniform grain sizes of JSC Mars-1 and fine sand (Table 1). As for creep, accelerated video playback speeds facilitate observation of these small (1–2 particle diameters) movements which occurred over the entire extent of the slope. As for tumbling ice particles, tumbling sediment neither moved substantial volumes of material, nor did it trigger other sediment movements

Regolith-specific results

JSC Mars-1 sediment movement types

JSC Mars-1 was the most active of the three regolith simulants. Discrete granular flows were detected for all but the one run with the gentlest initial slope angle (11.4 ± 0.1° for run 9 in Table 4). Creep was detected in 10 of the 16 runs with JSC Mars-1; and gas entrainment was observed in all but one run (run 12 in Table 4). Correlating sediment movements (Table 4) with the initial slope angle of the corresponding slope zone (Fig. 4a), discrete flow initiation was identified on slopes between 12.2° and 39.5°, while creep initiated on slopes between 11.4° and 33.9° (Table 3). The observed behaviour of discrete granular flows revealed a dependence on initial slope angle. For JSC Mars-1, run 9 (Table 4), with an initial slope angle of *c.* 10°, was the only run that did not display any discrete flow events. Flows became both larger and more numerous with increasing steeper slope angles. The maximum width of flows increased with initial slope angle from *c.* 1 cm at 15° slopes, and reaching the full slope width (*c.* 20 cm) for initial slopes of 20°. All runs starting at the AOR displayed discrete flows up to the full width of the slope, with runouts from crest to the bottom limit of the box. Maximum runouts started at less than 2 cm for 15° slopes and increasing to 6 cm at 17.5° initial slopes. For initial slopes below 20°, flows primarily took the form of slumps, leaving an upslope recess and a downslope berm of displaced sediment just below the recess. At steeper angles, flows appeared to skim, rather than slide over, the downslope surface, particularly flows starting at the

AOR. For these steepest runs, flows frequently initiated at the crest, leaving a sharp break of slope, which receded with continued flow activity.

As seen in Table 4, creep was detected in runs covering the full span of tested initial slope angles (10° to *c.* 30°). Conspicuously, creep was not detected for any of the runs starting at 20°. With the exception for run 9 (Table 4), creep was not detected in the crest zone (Fig. 4a), and in that instance, was only present at the edges, adjacent to the box. Gas entrainment activity was relatively independent of slope angle, except where it modified deposits from previously transported sediment.

JSC Mars-1 morphology observations

Slope failures on JSC Mars-1 slopes produced a variety of morphological changes on the surface. Discrete slope failures leave clearly defined areas of erosion and deposition, with distinct boundaries (Fig. 6). While the steepness of crest regions near the top of the slope did generally decrease, sharp breaks in slope were maintained through crest retreat, observed in several runs. Scarp-like features were frequently observed on eroded slope faces (Fig. 6a, b). For larger volumes, discrete slope failures, eroded material was carried to the bottom of the slope, colliding with the end of the test section with sufficient energy to create large clouds of dust, briefly obscuring the entire slope. Centimetre-scale puffs of dust, entrained by jets of escaping subsurface gas, were also observed. The timing of these events is difficult to constrain, given their brief duration and small scale, combined with near-vertical camera angles. Broadly, they occurred within the periods of gas entrainment activity listed in Table 4, beginning as early as the onset of sublimation up to halfway (48%) through the period, and ending from 32% to 98% through the sublimation period (Table 4). Jets adjacent to the box sides left remnant fans of dust just above the slope on the box sides (Fig. 6c). Escaping gas also left behind relatively large areas of pitting with millimetre-scale pores, principally at the foot of the slope where surface frost was buried by deposition (Fig. 6e), and also centred above one or both thermocouple trees (Figs 4a & 6d).

Looking at the difference raster on the right in Figure 7b, the greatest amount of erosion was on the right-hand side of the slope, at and below the original crestline, visible as the darker orange region. Deposition is deepest at the base slope zone (dark blue) and extends into the mid-slope zone, relatively symmetrically along the centreline. The difference raster on the left in Figure 8b shows the accumulation of frost at $t = 0$ min, the start of sublimation. However, over the majority of the slope, the thickness of the condensed frost is on the order of the photogrammetric noise. Hence, the pattern of

Table 3. *Slope angle, elevation and volume changes*

Run ID	Sediment	Nominal slope angle (°)	Base slope angle			Mid-slope angle			
			Initial (°)	Final (°)	Change (°)	Initial (°)	Final (°)	Change (°)	Initial (°)
1	Fine sand	10	10.21 ± 0.07	10.60 ± 0.08	0.39 ± 0.10	11.97 ± 0.09	11.80 ± 0.08	−0.17 ± 0.12	12.64 ± 0.09
2	Fine sand	15	14.28 ± 0.09	14.22 ± 0.09	−0.06 ± 0.13	16.94 ± 0.11	16.60 ± 0.10	−0.34 ± 0.15	22.33 ± 0.14
3	Fine sand	20	23.33 ± 0.23	24.27 ± 0.24	0.94 ± 0.34	21.98 ± 0.22	21.68 ± 0.22	−0.30 ± 0.31	22.43 ± 0.22
4	Fine sand	25	23.15 ± 0.21	22.94 ± 0.21	−0.21 ± 0.30	23.34 ± 0.21	22.95 ± 0.21	−0.39 ± 0.30	23.08 ± 0.21
5	Fine sand	25	25.76 ± 0.18	25.88 ± 0.18	0.12 ± 0.26	24.33 ± 0.17	24.07 ± 0.17	−0.26 ± 0.24	25.53 ± 0.18
6	Fine sand	AOR	34.02 ± 0.61	32.51 ± 0.58	−1.51 ± 0.84	30.97 ± 0.55	30.43 ± 0.54	−0.54 ± 0.78	32.97 ± 0.59
7	Fine sand	AOR	34.91 ± 0.32	30.47 ± 0.28	−4.44 ± 0.42	30.43 ± 0.28	30.50 ± 0.28	0.07 ± 0.39	31.23 ± 0.28
8	Fine sand	AOR	31.07 ± 0.96	25.32 ± 0.79	−5.75 ± 1.24	31.01 ± 0.96	27.58 ± 0.86	−3.43 ± 1.29	29.07 ± 0.90
9	JSC Mars-1	10	9.54 ± 0.07	8.81 ± 0.06	−0.73 ± 0.09	11.44 ± 0.08	11.16 ± 0.08	−0.28 ± 0.11	15.45 ± 0.11
10	JSC Mars-1	15	13.18 ± 0.09	13.86 ± 0.09	0.68 ± 0.13	14.46 ± 0.10	14.45 ± 0.10	−0.01 ± 0.14	15.94 ± 0.11
11	JSC Mars-1	15	12.08 ± 0.08	11.91 ± 0.08	−0.17 ± 0.11	15.21 ± 0.10	15.20 ± 0.10	−0.01 ± 0.14	16.58 ± 0.11
12	JSC Mars-1	15	17.24 ± 0.21	17.22 ± 0.21	−0.02 ± 0.29	17.87 ± 0.22	17.54 ± 0.21	−0.33 ± 0.30	23.79 ± 0.29
13	JSC Mars-1	17.5	22.99 ± 0.24	20.81 ± 0.22	−2.18 ± 0.32	18.29 ± 0.19	18.61 ± 0.19	0.32 ± 0.27	21.86 ± 0.23
14	JSC Mars-1	17.5	21.27 ± 0.18	18.86 ± 0.16	−2.41 ± 0.24	16.94 ± 0.14	17.42 ± 0.15	0.48 ± 0.20	17.60 ± 0.15
15	JSC Mars-1	17.5	18.06 ± 0.09	17.65 ± 0.09	−0.41 ± 0.13	18.27 ± 0.10	17.86 ± 0.09	−0.41 ± 0.13	18.71 ± 0.10
16	JSC Mars-1	17.5	14.65 ± 0.13	17.17 ± 0.15	2.52 ± 0.20	17.78 ± 0.16	17.34 ± 0.15	−0.44 ± 0.22	14.64 ± 0.13
17	JSC Mars-1	20	23.42 ± 0.21	20.44 ± 0.19	−2.98 ± 0.28	18.07 ± 0.17	17.89 ± 0.16	−0.18 ± 0.23	14.42 ± 0.13
18	JSC Mars-1	20	18.85 ± 0.30	14.63 ± 0.23	−4.22 ± 0.38	19.17 ± 0.31	19.17 ± 0.31	0.00 ± 0.43	12.17 ± 0.20
19	JSC Mars-1	20	22.00 ± 0.28	18.91 ± 0.24	−3.09 ± 0.37	17.00 ± 0.22	16.45 ± 0.21	−0.55 ± 0.30	16.90 ± 0.22
20	JSC Mars-1	AOR	23.20 ± 0.18	16.93 ± 0.13	−6.27 ± 0.22	34.06 ± 0.26	27.36 ± 0.21	−6.70 ± 0.34	39.53 ± 0.30
21	JSC Mars-1	AOR	24.96 ± 0.28	9.96 ± 0.11	−15.00 ± 0.30	26.56 ± 0.30	28.36 ± 0.32	1.80 ± 0.43	22.25 ± 0.25
22	JSC Mars-1	AOR	22.53 ± 0.33	8.58 ± 0.13	−13.95 ± 0.35	27.47 ± 0.40	24.51 ± 0.36	−2.96 ± 0.54	27.52 ± 0.40
23	JSC Mars-1	AOR	23.88 ± 0.47	5.76 ± 0.11	−18.12 ± 0.49	25.04 ± 0.50	21.33 ± 0.42	−3.71 ± 0.65	23.87 ± 0.47
24	JSC Mars-1	AOR	31.66 ± 0.22	19.60 ± 0.14	−12.06 ± 0.26	29.35 ± 0.20	16.36 ± 0.11	−12.99 ± 0.23	35.60 ± 0.25
25	Coarse sand	AOR	n.d.	n.d.	n.d.	n.d.	n.d.	n.d.	n.d.
26	Coarse sand	AOR	30.79 ± 0.49	30.00 ± 0.48	−0.79 ± 0.68	33.79 ± 0.54	31.98 ± 0.51	−1.81 ± 0.74	32.51 ± 0.52

n.d., No data.

frost, clearly visible in the corresponding orthophoto at $t = 0$ min (Fig. 7a), is not readily visible in the difference raster. The crest of the slope remains well defined and retreats, as seen in the orthophotos (Fig. 7a) and the long profiles (Fig. 7c). A small, arcuate alcove is clearly visible in the centre of the crest, along with lobate debris aprons downslope at $t = 80$ min. (Fig. 7a, b).

By way of comparison, Figure 8a–c illustrates the slope evolution for run 14 (JSC Mars-1 at 17.5°), the gentlest slope tested with substantial regolith movement (Table 2). In Figure 8a & c, we see that, unlike run 20 in Figure 7a–c, the initial slope is relatively smooth, with no break of slope at the crest, and curvature at the toe of the slope is confined to the bottom *c.* 30 mm (Fig. 8c), v. *c.* 100 mm for run 20 (Fig. 7c). The colour classifications representing slope elevation changes are repeated from Figure 8b to illustrate the relative magnitudes of slope modifications between the two runs. By comparison, all of the changes in run 14 are near the error estimates for elevation change of ±0.69 mm (Table 3). Although not readily apparent in Figure 8a, visual observation of the video recordings confirms the location and approximate magnitude of the long profiles in Figure 8c. Where essentially the entire slope was modified in the steeper run 20, only the lower half of run 14 underwent substantial alteration.

Quantitative results for JSC Mars-1

JSC Mars-1 was the most active of the three regolith types tested, undergoing the largest changes in slope elevations, volumetric displacement and the largest slope angle changes for all three slope zones (base, mid-slope and crest; Table 3). The maximum elevation change associated with erosion was 47 mm, with a mean of 2.3 mm; and the maximum change owing to deposition was 42 mm, with a mean of 3.0 mm (Table 3). The limit of detection for changes in slope height (ΔZ) is 1.4 mm, based on the noise estimates described under Controls and Error Estimation. The maximum erosional volume was 374 cm^3, with a mean of 60 cm^3, and the maximum depositional volume was 482 cm^3, with a mean of 82 cm^3 (Table 3). The mean decrease in base slope zone angle was 4.9°, with a maximum of 15°. Both the mid-slope and crest zones had a mean decrease in slope of 1.6°, with maximum reductions of 13° and 15°, respectively (Table 3).

Fine sand sediment movement types

Fine sand transport was only detected in the three runs starting at the AOR (Table 4). For the first run (run 6 in Table 4), sediment movement was almost imperceptible. The cumulative magnitude of the

Crest slope angle		Elevation change			Volumes			
Final (°)	Change (°)	Erosion (mm)	Deposition (mm)	Mean (mm)	Regolith total (cm³)	Erosion (cm³)	Deposition (cm³)	Frost (cm³)
12.66 ± 0.09	0.02 ± 0.13	−4.00 ± 0.57	11.00 ± 0.57	−0.05 ± 0.04	3622 ± 26	14.87 ± 0.11	13.38 ± 0.10	33.49 ± 0.24
21.60 ± 0.13	−0.73 ± 0.19	−6.00 ± 0.47	0.00 ± 0.47	−0.24 ± 0.01	3276 ± 20	10.63 ± 0.07	0.00 ± 0.00	16.52 ± 0.10
22.62 ± 0.23	0.19 ± 0.32	−4.00 ± 0.82	0.00 ± 0.82	−0.20 ± 0.01	3154 ± 32	7.55 ± 0.08	0.00 ± 0.00	19.07 ± 0.19
22.68 ± 0.21	−0.40 ± 0.30	−3.00 ± 0.64	6.00 ± 0.64	0.44 ± 0.02	2712 ± 25	1.69 ± 0.02	17.72 ± 0.16	51.89 ± 0.47
24.56 ± 0.17	−0.97 ± 0.25	−3.00 ± 0.54	7.00 ± 0.54	0.10 ± 0.02	3478 ± 25	4.61 ± 0.03	11.91 ± 0.08	79.96 ± 0.57
29.26 ± 0.52	−3.71 ± 0.79	−8.00 ± 1.32	5.00 ± 1.32	−1.56 ± 0.03	3391 ± 61	75.92 ± 1.36	1.55 ± 0.03	20.28 ± 0.36
30.93 ± 0.28	−0.30 ± 0.40	−7.00 ± 0.59	23.00 ± 0.59	−0.49 ± 0.07	3057 ± 28	69.13 ± 0.62	42.36 ± 0.38	12.76 ± 0.12
33.62 ± 1.04	4.55 ± 1.38	−12.00 ± 2.29	16.00 ± 2.29	0.91 ± 0.06	3471 ± 108	88.85 ± 2.75	131.14 ± 4.07	37.97 ± 1.18
14.60 ± 0.11	−0.85 ± 0.15	−5.00 ± 0.58	3.00 ± 0.58	0.06 ± 0.02	3322 ± 24	2.84 ± 0.02	5.34 ± 0.04	1.01 ± 0.01
15.74 ± 0.11	−0.20 ± 0.15	−7.00 ± 0.54	4.00 ± 0.54	−0.05 ± 0.02	4158 ± 28	12.84 ± 0.09	1.46 ± 0.01	4.28 ± 0.03
16.43 ± 0.11	−0.15 ± 0.16	−4.00 ± 0.57	0.00 ± 0.57	−0.23 ± 0.01	4296 ± 29	6.58 ± 0.04	0.00 ± 0.00	20.37 ± 0.14
23.50 ± 0.28	−0.29 ± 0.40	−6.00 ± 1.00	0.00 ± 1.00	−0.39 ± 0.01	3872 ± 47	23.43 ± 0.28	0.00 ± 0.00	45.43 ± 0.55
20.86 ± 0.22	−1.00 ± 0.32	−13.00 ± 0.83	5.00 ± 0.83	−0.11 ± 0.04	3949 ± 41	17.95 ± 0.19	15.68 ± 0.16	3.98 ± 0.04
16.67 ± 0.14	−0.93 ± 0.20	−8.00 ± 0.69	14.00 ± 0.69	0.87 ± 0.05	3672 ± 31	25.08 ± 0.21	8.22 ± 0.07	11.46 ± 0.10
16.81 ± 0.09	−1.90 ± 0.13	−4.00 ± 0.43	11.00 ± 0.43	1.46 ± 0.03	4055 ± 21	0.00 ± 0.00	67.44 ± 0.35	113.06 ± 0.59
15.10 ± 0.13	0.46 ± 0.19	−6.00 ± 0.72	8.00 ± 0.72	−0.81 ± 0.03	3995 ± 35	1.57 ± 0.01	20.03 ± 0.18	27.76 ± 0.25
12.16 ± 0.11	−2.26 ± 0.17	−8.00 ± 0.70	8.00 ± 0.70	−0.47 ± 0.04	3477 ± 32	19.46 ± 0.18	14.57 ± 0.13	4.02 ± 0.04
12.61 ± 0.20	0.44 ± 0.28	0.00 ± 0.71	9.00 ± 0.71	1.40 ± 0.02	2302 ± 35	30.17 ± 0.46	78.36 ± 1.20	18.47 ± 0.28
16.48 ± 0.21	−0.42 ± 0.30	0.00 ± 0.55	6.00 ± 0.55	0.88 ± 0.01	2102 ± 27	2.40 ± 0.03	72.66 ± 0.93	56.83 ± 0.73
30.20 ± 0.23	−9.33 ± 0.38	−18.00 ± 0.79	18.00 ± 0.79	0.92 ± 0.08	4779 ± 37	150.43 ± 1.16	187.60 ± 1.44	113.61 ± 0.87
23.17 ± 0.26	0.92 ± 0.36	−9.00 ± 0.95	14.00 ± 0.95	−0.55 ± 0.05	4054 ± 45	78.06 ± 0.87	45.59 ± 0.51	n.d.
29.13 ± 0.43	1.61 ± 0.59	−13.00 ± 1.32	24.00 ± 1.32	0.34 ± 0.08	4737 ± 69	136.92 ± 2.01	154.34 ± 2.26	41.95 ± 0.62
27.54 ± 0.55	3.67 ± 0.72	−13.00 ± 1.37	24.00 ± 1.37	2.11 ± 0.09	2917 ± 58	78.73 ± 1.56	157.71 ± 3.12	108.01 ± 2.14
20.64 ± 0.14	−14.96 ± 0.28	−47.00 ± 0.55	42.00 ± 0.55	2.33 ± 0.21	3726 ± 26	373.81 ± 2.58	481.96 ± 3.32	37.15 ± 0.26
n.d.	n.d.	n.d.	n.d.	n.d.	n.d.	n.d.	n.d.	n.d.
32.26 ± 0.51	−0.25 ± 0.73	−5.00 ± 1.20	15.00 ± 1.20	0.50 ± 0.05	3605 ± 57	9.98 ± 0.16	32.23 ± 0.51	64.80 ± 1.03

minute creep observed along the retreating boundaries of surface frost was only revealed in the photogrammetric results (Table 3). For the second run (run 7 in Table 4), slow, steady creep eventually led to a large, slope-wide discrete flow. This was the only run with fine sand that exhibited gas entrainment, which in this case was observed as bubbling of the sediment deposited atop surface frost at the toe of the slope. This event which lasted c. 139 s, was an immediate consequence of a discrete flow, which over-topped an accumulation of surface frost at the toe of the slope, just over halfway through the c. 2 h run (Table 4). For the third run (run 8 in Table 4), a single large discrete flow was accompanied by creep, which was most evident in the reshaping of the depositional fan generated by the initial, discrete flow event. For these three runs, the initial slope angle was photogrammetrically measured between 27.6° and 30.5° (Table 3). Discrete flows and creep were correlated with photogrammetrically determined slope angles, each between 29° and 35° (Tables 3 & 4).

Fine sand morphology observations

Morphological changes of fine sand slopes were restricted to erosional lowering of steeper slope segments and development of depositional fans. Run 8,

the most active of the fine sand runs, underwent the greatest slope angle reduction for all three slope zones (Fig. 4a and Table 3). As illustrated in Figure 9c, roughly the top third of the long profile was eroded, while the balance of the slope accumulated the associated deposition. Both the pre-frost and t = 100 min profiles highlight the somewhat featureless character of the sand slope. The t = 100 min orthophoto in Figure 9a does reveal somewhat extensive depositional features over much of the slope. The t = 100 min profile, recorded along the slope centreline, fails to capture the full depth of erosion visible at the left-hand side of the crest in the difference raster (Fig. 9b). Noting that interference of the box at the toe of the slope limits interpretation of run-out features, depositional material did, in some instances, accumulate along the upslope boundary of dense surface frost without reaching the box boundary. Subsequent sublimation of this frost left steepened lobate termini.

In comparison with the JSC Mars-1 runs, fine sand slopes remained relatively smooth, with no sharp breaks or scarps. Fine sand did, in contrast, develop more complex depositional features, fans frequently colliding and coalescing (Fig. 9a). Entrainment features were much less evident than for JSC Mars-1, only one entrainment event being observed.

Table 4. *Observed sediment transport types*

Run ID	Regolith simulant	Initial slope angle (°)	Discrete flow		Creep		Gas entrainment		Grain tumbling	
			Timing (s)	Areas	Timing (s)	Areas	Timing (s)	Areas	Timing (s)	Areas
1	Fine sand	10								
2	Fine sand	15								
3	Fine sand	20								
4	Fine sand	25								
5	Fine sand	25								
6	Fine sand	AOR			30–6720	Mid and crest edges				
7	Fine sand	AOR	2509–4007	Centre, base	3483–5952	Full width, mid	3880–4019	Toe bubbling		
8	Fine sand	AOR	588–666	Crest-toe	312–5979	Crest-toe				
Control*	Fine sand	AOR								
9	JSC Mars-1	10			166–913	Mid and crest edges	373–5589	Crest TC tree		
10	JSC Mars-1	15	174–420	Lower mid; crest TC[†] tree	42–1112	Mid; along frost edges	252–5962	Crest and mid TC tree; eroded and slumped areas		
11	JSC Mars-1	15	60–186	Mid	810–1260	Mid and base	60–6055	TC trees and proximal; along frost edges		
12	JSC Mars-1	15	5236–5237	Mid; RHS mid	155–5368	Base; upper mid				
13	JSC Mars-1	17.5	18–574	Crest and mid	171–1058	Base deposits	0–6367	Crest along frost edge; vigorous boiling toe deposits		
14	JSC Mars-1	17.5	32–780	Mid			171–6257	Crest TC tree; base and toe		

15	JSC Mars-1	17.5	682–6049	Mid; mid and crest	99–5219	Mid	444–6065	Upper TC tree; mid TC tree		
16	JSC Mars-1	17.5	41–6651	Mid and crest	0–789	Mid and base	44–6541	Crest and mid TC trees		
17	JSC Mars-1	20	240–4625	Mid and sink holes RHS			490–8106	Toe and crest TC tree; RHS mid		
18	JSC Mars-1	20	140–2181	Crest; crest, mid and base			231–6060	Base deposits; mid TC tree		
19	JSC Mars-1	20	162–547	Mid and LHS crest			369–6051	Mid frost edge; toe and base deposits		
20	JSC Mars-1	AOR	317–2997	Crest; mid and base	2989–4354	Mid and base	883–4354	Toe deposits		
Control*	JSC Mars-1	AOR								
21	JSC Mars-1	AOR	124–3777	Mid; mid and crest			2482–2496	Toe deposits		
22	JSC Mars-1	AOR	333–5018	Mid to crest			335–5159	Toe dust deposits; base deposits		
23	JSC Mars-1	AOR	168–6500	Mid; mid and crest	570–4863	Base and mid	328–7187	Base and toe deposit pitting; mid eroded areas pitting		
24	JSC Mars-1	AOR	51–6762	Mid; crest	189–6762	Mid, base and toe	3821–6762	Base and toe boiling deposits; crest to toe pitting		
25	CsAORr1	AOR	1560–1563	RHS mid (ice)	1563–7320	Mid and crest			0–6880	Entire slope
26	CsAORr2	AOR	4702–4703	RHS mid	1000–5193	Base, mid and crest edges			0–5193	Entire slope

Notes: Empty cells indicate no observed activity.
*Initial slope angle based on mid-slope zone (Fig. 4a). Control run (no CO₂ admitted to chamber).
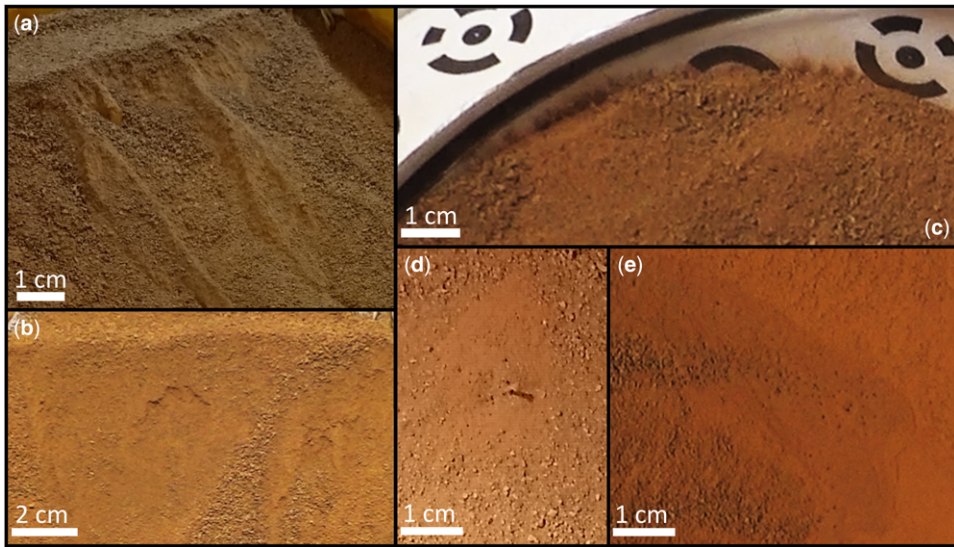†TC, Thermocouple.

Fig. 6. Resultant slope morphologies. (**a**) Oblique view of the crest slope zone of Run 20 (Table 3) displaying scarp and ridge morphology at the end of the experimental run. The clearly defined areas of failure, delimited by fresh scarps faces at the slope crest, parallel ridges to either side and debris aprons, are typical of the observed discrete sediment flows. (**b**) Overhead view of a small scarp which formed *c.* 2 cm below the slope crest from (run 23 Table 3). (**c**) Dust fans along back wall of box are the result of centimetre-scale jets of escaping CO_2 gas carrying entrained dust (from run 18 Table 3). (**d**) Pitting around the mid-slope thermocouple tree (upper-most thermocouple has been exposed at the surface), caused by escaping CO_2 gas (from run 15 Table 3). (**e**) Pitting at the base slope zone from run 24 (Table 3).
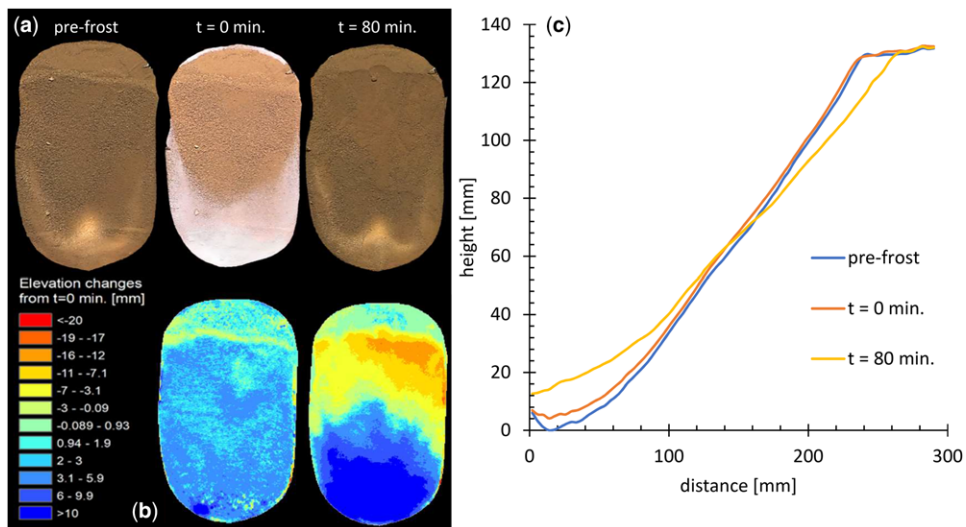
Fig. 7. Slope evolution for run 20 (JSC Mars-1 at AOR): (**a**) orthophotos showing visible appearance of the surface prior to frost condensation, at $t = 0$ (the start of sublimation), $t = 80$ min (the end of sublimation). At $t = 0$, surface frost is clearly visible as a white beard on the lower half of the slope, and as a smaller, dense accumulation at the back edge of the slope, adjacent to the box. (**b**) Difference rasters illustrating topographic changes between the pre-frost slope and the slope at the start and end of sublimation. Red represents erosion and blue represents deposition. Both the orthophotos and the difference rasters are oriented with the slope crest at the top of each image. (**c**) Evolution of the topographic long profiles for the slope pre-frost, and at the start and end of sublimation. The slope zones used to measure the slope angles are indicated in Figure 4a.
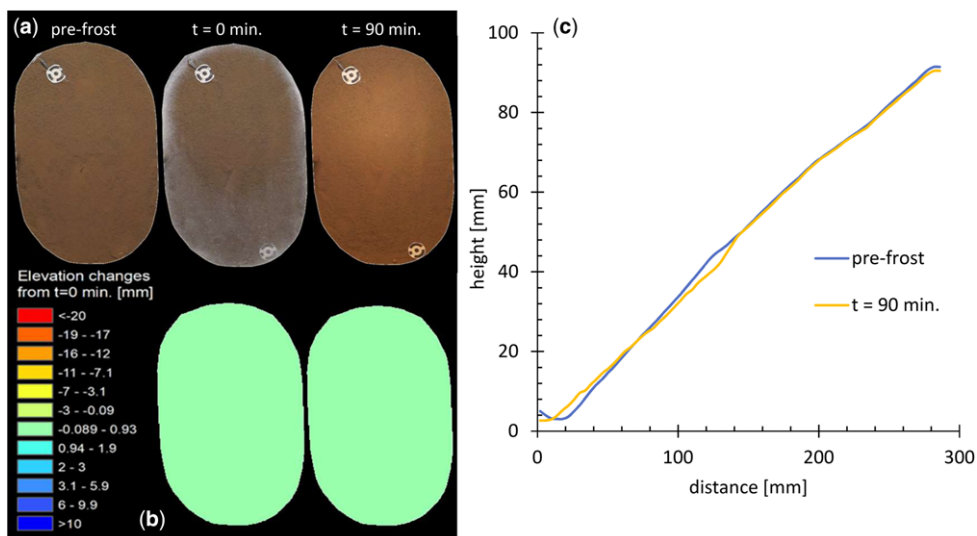
Fig. 8. Slope evolution for run 14 (JSC Mars-1 at 17.5°): (**a**) orthophotos showing visible appearance of the surface prior to frost condensation, at $t = 0$ min (the start of sublimation), $t = 90$ min (the end of sublimation). At $t = 0$ min, a white beard of surface frost is clearly visible on the base slope zone, a thin (1–2 cm) concentration of frost encircling the balance of the slope along the box edges. (**b**) Difference rasters illustrating topographic changes between the pre-frost slope and the slope at the start and end of sublimation. The colour classifications representing elevation changes are the same as those in Figure 7. The singular classification illustrates that the scale of slope modifications was much smaller than that of run 20, in Figure 7. (**c**) Evolution of the topographic long profiles for the slope pre-frost, and at the start and end of sublimation. The slope zones used to measure the slope angles are indicated in Figure 4a.
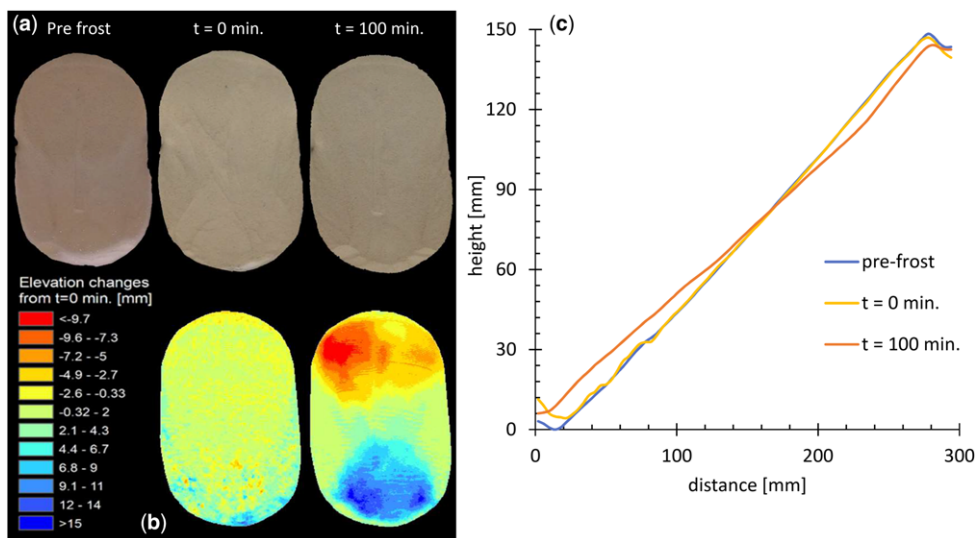

Fig. 9. Slope evolution for run 8 (fine sand at AOR): (**a**) orthophotos showing visible appearance of the surface prior to frost condensation, at $t = 0$ (the start of sublimation), $t = 80$ min (the end of sublimation). At $t = 0$, surface frost is clearly visible at the toe of the slope, and faintly visible on the lower half of the slope and along the edges of the box. (**b**) Difference rasters illustrating topographic changes between the pre-frost slope and the slope at the start and end of sublimation. Red represents erosion and blue represents deposition. Both the orthophotos and the difference rasters are oriented with the slope crest at the top of each image. (**c**) Evolution of the topographic long profiles for the slope pre-frost, and at the start and end of sublimation. The slope zones used to measure the slope angles are indicated in Figure 4a.

Fine sand quantitative results

For the three active fine sand runs (all at the angle of repose, Table 2), the maximum change in slope elevation associated with erosion was 12 mm, with a mean of 9.0 mm, compared with a maximum of 47 mm and mean of 10 mm for JSC Mars-1. The maximum change associated with deposition was 23 mm, with a mean of 15 mm, compared with a maximum of 42 mm and mean of 12 mm for JSC Mars-1 (Table 3). The fine sand slopes underwent 68.7–88.8 cm^3 of erosion, with a mean of 77.8 cm^3. Deposition was between 1.55 and 132.0 cm^3, with a mean of 59.8 cm^3 (Table 3). The mean change of angle for the base slope zone was −3.9°. The mid-slope and crest zones were essentially unchanged, the measured values (−1.3° and 0.5° respectively) being well within the estimated error of ±1.4° (Table 3). The largest slope angle changes were 4.6°, −3.4° and −5.75° for the crest, mid-slope and base regions respectively – all of these values coming from run 8 (Table 3).

Coarse sand

Coarse sand sediment movement types

Coarse sand was the least active of the three regolith simulants tested. Only two runs, both at the AOR were conducted with coarse sand, as no appreciable sediment transport was observed. Poor camera placement prevented development of a usable photogrammetric model for run 25; however, minute surface alterations were observed, visually. In that run, a single, shallow (<2 mm deep) discrete sediment flow (*c.* 10 mm wide, 20 mm long) was observed, apparently driven downslope by a similarly small mass of surface frost which broke away from the side of the test section. Creep can be detected along the retreating edges of surface frost in the video recordings. Larger sediment grains can also be seen to roll or tumble in the video recordings. While this activity is more easily observed than the creep, it does not appear to cause any substantial slope movement.

A single discrete slope failure was observed in run 26, over halfway through the sublimation process; in this case without the influence of frost falling from the box side. The extent of the sediment transport was comparable with that in run 25, and had a similarly limited effect on the surface morphology. As for run 25, rolling and tumbling of larger sediment grains was active throughout the duration of the run, widely distributed across the entire slope. Based on photogrammetric results, the discrete regolith flow was detected between 30° and 32°, and creep was detected at 30°.

Coarse sand morphological and quantitative results

Only superficial morphological changes were observed for both coarse sand runs. Both runs displayed the tumbling of individual sediment grains. These grains were visually estimated to comprise <5% of all surface grains, distributed widely and uniformly across the entire slope area. These sub-centimetre-scale movements produced no discernible surface features on either of the two coarse sand slopes. Creep was visible across the mid and crest slope zones for run 25, with somewhat more evident movement along the box boundaries. Creep was less widespread in run 26 than in run 25, only apparent along the box edges and in association with the retreating edge of surface frost accumulations. For both runs, creep-induced movements were too small to produce photogrammetrically detectable surface alterations.

Coarse sand, initially at the nominal angle of repose, showed no substantial changes of elevation: on average <1 mm for the entire slope (Table 3), which is less than the estimated vertical photogrammetric noise of 1.2 mm (Table 3). The measured erosion for run 26 was 10.0 cm^3 (0.3% of the total regolith volume), while deposition was 32.2 cm^3 (0.9% of the total regolith volume) and the volume of frost was 64.8 cm^3 (Table 3). To put these volumes in context, the erosion and deposition were 0.3% and 0.9% of the total regolith volume, respectively. Remaining surface frost, visible in the final image pair for run 26, is included in the reported deposition volume. The mean change of slope angle was −3.21 ± 0.73° for the base slope zone, −0.6 ± 0.66° for the mid-slope zone and −3.4 ± 0.37° for the crest zone (Table 3).

Discussion

Sylvest *et al.* (2016) proposed that the observed mass-wasting behaviour of slopes of JSC Mars-1, initially at the angle of repose, was triggered by the sublimation of CO_2 frost condensed within the regolith pore space. They hypothesized that the rapid production of gas produced via sublimation caused the pore pressure within the sediment to increase and therefore initiated failure. In this work, we have tested two new substrate types and different initial slope angles, and we found:

(1) volumes of sediment moved by JSC Mars-1 remaining similar down to slope angles of 20° (and are slightly reduced at 17°) and volumes of sediment moving in fine sand experiments of the same magnitude, but only near the angle of repose (little movement was

detected at other initial angles) and only very limited sediment transport occurring for coarse sand near the angle of repose;

(2) four different types of sediment movement, discrete flow, creep, gas entrainment and grain tumbling (creep was not reported by Sylvest *et al.* 2016).

In the following discussion, we integrate our experimental results into a discussion of the physics of these movements and then discuss their applicability to Mars. Our discussion focuses on the discrete and creep flows, as these cause the most sediment transport.

Mechanism and physics

In order to assess whether the mass wasting we observe in our experiments is caused by the reduction in friction angle of the sediment owing to the gas flow reducing the intergranular pressure, we consider a simple one-dimensional analytical model. The model solves continuity equations for energy and CO$_2$, and balances downslope gravitational attraction against Coulomb friction.

Suppose that the bed comprises sand with bulk density ρ_s, thermal conductivity κ, permeability k, specific heat capacity c and some initial amount of CO$_2$ ice with density ρ_i. We assume that at $t = 0$ the bed is all at the sublimation temperature T_s, and then a radiant heat flux Q is applied to the surface. We measure distance downwards normal to the surface using the coordinate x, and define the point $X(t)$ as the boundary between CO$_2$ ice and pure sand. Initially $X(0) = 0$, but over time, as heat is conducted into the bed, this point will move downwards (increasing x). We assume that the heat flux is due only to heat conduction between the sand grains; thus the temperature $T(t, x)$ satisfies the equation

$$\rho_s c T_t = \kappa T_{xx}, \quad 0 < x < X(t), \quad (1)$$

where the subscripts t and x are partial derivatives with respect to time and position.

The boundary conditions are

$$Q + \kappa T_x(t,0) = 0 \quad \text{and} \quad T(t,X(t)) = T_s, \quad (2)$$

representing the heat flux at the surface, the temperature being at the sublimation temperature at the CO$_2$ ice interface. The movement of the point $X(t)$ is given by a differential equation that describes the heat flux driving the sublimation of the CO$_2$ ice:

$$e\rho_i \dot{X}(t) + \kappa T_x(t,X(t)) = 0, \quad (3)$$

where e is the enthalpy of sublimation. We assume that temperature variations do not significantly affect any material properties, including the carbon dioxide gas density ρ_g. The behaviour of the solution is best understood by defining the following time, length and temperatures scales, $t^* = \left(\kappa \rho_i^2 e^2 / \rho_s c Q^2\right)$, $x^* = (\kappa \rho_i e / \rho_s c Q)$ and $T^* = (\rho_i e / \rho_s c)$. The model is then non-dimensionalized by writing

$$X(t) = x^* f\left(\frac{t}{t^*}\right), \quad (4)$$

and

$$T(t,x) = T_s + T^* g\left(\frac{t}{t^*}, \frac{x}{x^*}\right), \quad (5)$$

where f and g are non-dimensional functions. The resulting non-dimensional system and an approximate analytic solution are described in Appendix B. A key point is that, for time less than the order of t^*, most of the heat is going into sublimating ice, and the frost front advances linearly. Conversely, for time greater than t^*, the energy balance changes and most of the heat goes into warming ice-free sand, the flux decaying as $1/\sqrt{t}$.

The largest gas flux, and hence highest grain mobility, occurs for short values of time. A power series solution for f and g can be developed in non-dimensionalized time, which gives the frost point advance as

$$X(t) = x^* \left(\frac{t}{t^*}\right) - \frac{1}{2}\left(\frac{t}{t^*}\right)^2 + \frac{5}{6}\left(\frac{t}{t^*}\right)^3 + \cdots \quad (6)$$

Now, the mass production rate of CO$_2$ is $\rho_i \dot{X}$, and we assume that the gas density ρ_g is constant and equal to the value at the sublimation temperature T_s and background pressure p_0. The volume flux of CO$_2$ for $x < X(t)$ is therefore

$$q(t) = \frac{\rho_i}{\rho_g} \dot{X}(t) = \frac{\rho_i}{\rho_s} \frac{x^*}{t^*} f_s(s), \quad (7)$$

where the subscript s denotes the derivative. Within the bed, Darcy's law gives the stress on the sand grains as $S = (\nu/k)q(t)$. If we define the non-dimensional Darcy stress, $S^* = (\nu/k)(\rho_i/\rho_g)(x^*/t^*)$ $(1/\rho_s g) = (\nu Q/ke\rho_g \rho_s g)$, then $S = \rho_s g S^* f_s$, S being the reduction in normal stress due to the gas flow. As the maximum shear stress that can be supported by the grains is proportional to the normal stress between the grains, this reduction increases the probability of failure. The Coulomb failure criterion is

Table 5. *Analytical results for internal friction angle calculations*

Symbol	Terrestrial results			Martian results			Definition
	Fine sand	JSC Mars-1	Coarse sand	Fine sand	JSC Mars-1	Coarse sand	
t^* (s)	104	106	103	104	106	103	Scale time
x^* (mm)	4.3	4.3	4.2	4.3	4.3	4.2	Scale length
q (m s^{-1})	0.0123	0.0123	0.0123	0.0123	0.0123	0.0123	Volume flux of CO_2
$\Delta\theta$	1.9°	17.6°	0.46°	5.1°	50.3°	1.2°	Change of internal friction angle

independent of depth, and after dividing by $x\rho_s g$, at any point $x < X(t)$, it is

$$\sin \theta = \mu[\cos \theta - S^* f_s], \qquad (8)$$

where μ is the coefficient of friction and θ is the slope angle. Thus, it can be seen that S^* is the key non-dimensional group that determines whether the bed is likely to mobilize, and that this does not depend on the concentration of ice. The ice concentration will, however, determine how long mobilization will occur, owing to the dependence on t^*. For short times ($t < t^*$), $f_s = 1$; hence, the CO_2 flux can initially be calculated by assuming that all the radiant heat is subliming CO_2 ice.

Solving equation (8) for θ, using the parameters for the experimental conditions, gives the new, reduced internal friction angle for the slope under those conditions. This can be solved exactly, but an approximate formula, for small q, is more convenient:

$$\tan \theta = \mu\left[1 - \sqrt{1 + \mu^2}\, S^* f_s\right]. \qquad (9)$$

The input experimental parameters are listed in Table B1. If the model provides an accurate description of the physics, then we would expect that the reduction in friction angle corresponds to the initial slopes at which we observe movement in our experiments. Note however, that there is considerable (as much as 5°) stochastic variation in the failure angle of granular materials.

The results of applying our analytical model to our experimental data are presented in Table 5. Because coarse sand shows no significant transport, even at the angle of repose, this substrate is expected to have the lowest reduction in friction angle. Conversely, because JSC Mars-1 transports substantial volumes of sediment on slopes down to 17° (Table 3), it is expected to undergo the highest

reduction in friction angle. Fine sand should therefore be intermediate, between the other two sediments, as it only shows substantial volume transport near the angle of repose. The different substrates do have the expected relative reductions in friction angle predicted by the model (Table 5). The reduction in friction angles for coarse and fine sand under terrestrial gravity (0.5° and 1.9° respectively, Table 5) match our experimental results, whereby no appreciable movement is seen for coarse sand, and appreciable movement is only observed near the angle of repose for fine sand. We note that the finer grain fraction in the coarse sand did show some signs of mobilization; however, we infer that the presence of larger grains both impeded mass movement and also increased the substrate permeability, preventing the build-up of pressure within the pore space. For JSC Mars-1, we get a slightly larger change of internal friction angle than expected, of 17.6°. Based on our experimental results, this would imply activity in the 15° experiments, which was not observed. However, unlike fine and coarse sand, we did not make our own independent measurements of the permeability for the JSC Mars-1 material (Sizemore & Mellon 2008), and slight variations can change the outcome of the calculation. Equally, our measurements indicated that the bulk density of the JSC Mars-1 could vary by ± 0.07 g cm^{-3}, even with similar preparation, which could also contribute to this discrepancy. The volume flux velocity for our experiments was based on the rate of sublimation dictated by the supplied radiant heat and thermodynamic properties of the CO_2. As these parameters were held constant for all runs, the volume flux velocity was also constant, at 0.012 m s^{-1} (Table 5).

The scale time, t^*, is the cross-over time, when radiant heat input transitions from primarily subliming CO_2 frost to primarily heating the regolith. In practice, t^* is neither readily observed nor measured, but we might expect it to have the same order of magnitude as the duration of the phase
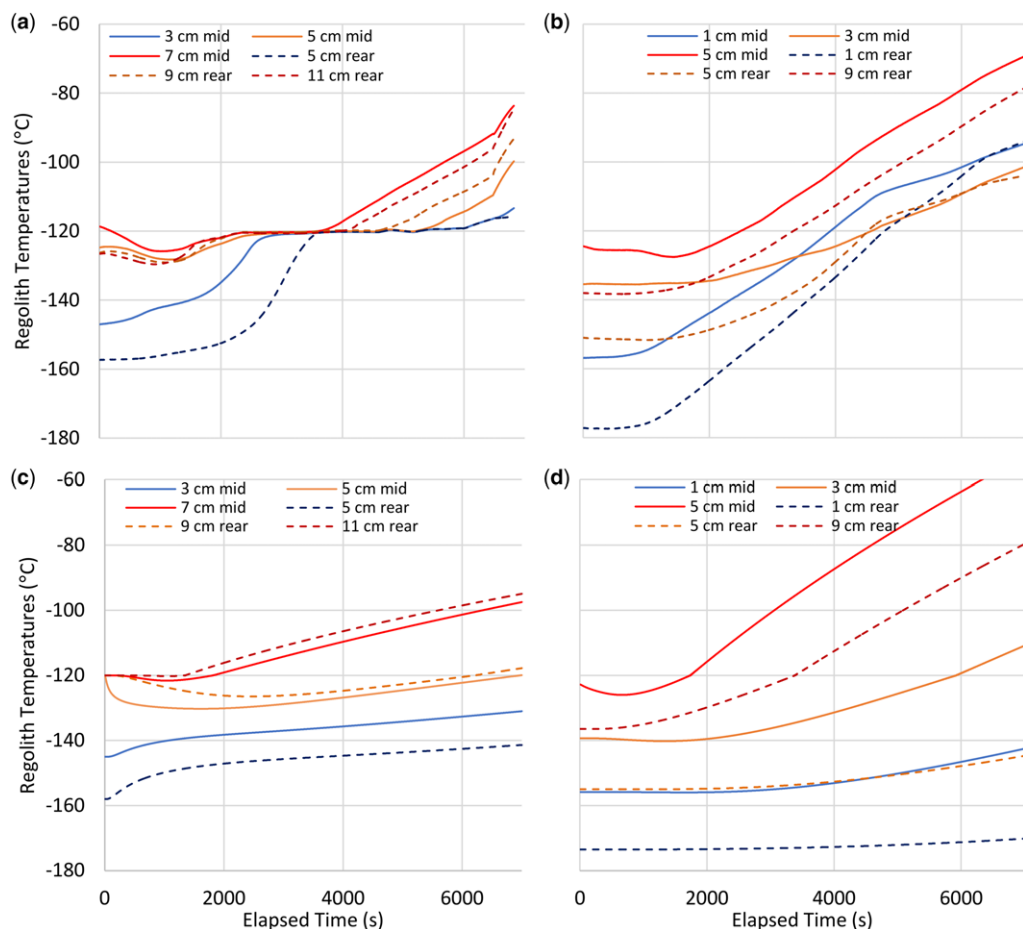
Fig. 10. Experimental and modelled temperature traces during sublimation. (**a**) Run 8 (fine sand at AOR). (**b**) Run 23 (JSC Mars-1 at AOR). (**c**) and (**d**) Simulations of the one-dimensional heat conduction equation with sublimation for fine sand and JSC Mars-1, respectively. Thermocouple locations are indicated in Figure 4a. Vertical positions are in centimetres above the bottom of the box. Solid lines correspond to mid-slope thermocouples; dashed rear. Blue traces correspond to the deepest locations; red traces are the closest to the slope surface and orange are in-between.

change. Example experimental temperature traces over the duration of sublimation for fine sand and JSC Mars-1, both initially near the angle of repose, are presented in Figure 10a & b. The longer scale time (t^*) output from our analytical model for JSC Mars-1 might be expected to be evidenced by a delayed start of regolith temperature increase, relative to fine sand. Neither of these predictions is borne out in the temperature data. In Figure 10a for fine sand, initially, the deepest parts of the slope begin to warm with the cessation of active cooling and the upper regions continue to cool. Each trace, roughly in order of increasing depth, warms to the sublimation temperature (c. −120°C), where it remains constant during sublimation of the

condensed frost before continuing to warm. The phase change dominates the temperature curves for hours, v. the <2 min suggested by t^* in our analytical model (Table 5). In contrast to fine sand, the behaviour of JSC Mars-1 is different (Fig. 10b). In this case, all six temperature traces are essentially constant at the onset of the sublimation process, followed by a steady increase. None of the JSC Mars-1 traces displays a plateau suggesting active frost sublimation, hence we cannot compare these data with the sublimation times of the fine sand runs, nor with the predicted t^* values from our analytical results.

An additional complication for understanding the experiments is the complicated geometry and initial

conditions. As shown in Figure 10, the initial temperature profile is far from uniform, and the entire bed is not at the sublimation temperature as was assumed in the analytical model. To investigate this further, we numerically solved the one-dimensional heat conduction equation with sublimation. We assumed zero heat flux on the lower boundary, and the same radiant heat flux used in the analytical model on the upper boundary (350 W m^{-2}, Table A1). The frost load was estimated to be 20 kg m^{-3}. We attempted a simple match of the initial temperature profile to the thermocouple readings. The results can be seen in Figure 10, along with the experimental traces. We see reasonable agreement between the experimental and numerical traces for JSC Mars-1 (Fig. 10b, d). The traces for fine sand (Fig. 10a, c) do not match, which suggests that, although the theory is reasonable, the uncertainties in the initial and boundary conditions substantially affect the energy budget, and thus the sublimation rate.

These null results highlight that the predictive power of these physical models is limited by the quality of the measured parameters, particularly the regolith properties. Thermal conductivity, for example, can vary by an order of magnitude depending on how the regolith was handled during preparation of the slope. JSC Mars-1 provides particularly difficult challenges for modelling, owing to the increased influence of inter-particle interactions compared with even fine sand. However, even with these caveats, we are able to obtain results which capture certain aspects of our experimental results, and that provide a better understanding of the basic physical mechanisms driving the sediment transport in our experiments. This then allows us to transfer our results to Mars, which we present in the following section.

Application to Mars

One of the underlying assumptions in the analytical models outlined above was that CO_2 ice is emplaced below or within the sediment, in order for sediment transport to occur. This reflects a key observation from both the experiments reported here and in Sylvest *et al.* (2016): sediment transport is only triggered where CO_2 frost is in the subsurface, and not where it has accumulated on the surface. Reporting of CO_2 ice on Mars is limited to surface observations of frost and/or slab ice (e.g. Gardin *et al.* 2010; Appéré *et al.* 2011; Piqueux *et al.* 2015). However, when surface CO_2 is not present, trapping of CO_2 ice within the regolith should be possible, as has been previously formulated for the emplacement of water ice in the subsurface (e.g. Mellon *et al.* 1993). Assuming Mars' regolith is dry, the atmosphere can diffuse into the subsurface pore space. The surface of Mars undergoes a diurnal and annual temperature cycle, and therefore the physical processes described in 'Mechanism and physics' section could take place repeatedly on time and depth scales concurrent with diurnal, annual and secular temperature variations. As the surface temperature variation propagates into the regolith, it experiences a lagging and damping effect (for illustration, see Hagermann 2005). This means that there are periods in the subsurface thermal cycle when the temperature wave decreases to below the sublimation point of CO_2 such that the CO_2 sublimation horizon moves upwards. As atmospheric CO_2 diffuses into the soil, subsurface CO_2 deposition occurs. At low pressures, this is best described as molecules following the vapour pressure gradient until they are deposited as ice at depth. Our experiments reveal that the nature of the CO_2 frost, and exactly where it ends up on or in the slope, should control the type and quantity of sediment transport owing to subsequent sublimation of the frost.

Although beyond the scope of the current study, temperature gradients through the depth of the slope, during the condensation phase of the experiments, are expected to control the depth of subsurface frost formation, and possibly the density of both subsurface and surface frost. Our analytical models demonstrate that these are key factors in determining whether sediment transport will occur.

Given these arguments, we believe that the emplacement of CO_2 into the regolith pore-space should be possible on Mars, and therefore, we have applied our simple analytical model above using Martian gravity instead of terrestrial (Table 4). This reveals that the reduction in friction angle should be even greater on Mars for any given substrate, compared with the reductions observed on Earth. Hence, these results should be applicable to a larger range of slopes for any given substrate than expected, based on our laboratory results without scaling. The calculations under Martian gravity suggest that movements in fine sand should be observable on slopes as much as 5° lower than the nominal angle of repose.

In summary, our results predict that mass wasting (creep and discrete granular flows) can be triggered by the sublimation of CO_2 frost on Mars, where temperatures in the near-surface regolith dip below the condensation temperature of CO_2, and where CO_2 surface frost or ice is not present at the surface when the sediment transport occurs. Our experiments do not allow us to directly compare morphologies observed on the Martian surface with morphologies observed in our experiments owing to the difference in scale. However, from our results we can infer likely locations on Mars where this process could occur by examining regions which have similar slopes and grainsizes to those found to be active in our experiments. Many of the present-day sediment transport events associated with Martian

gullies fall into this category. Notable exceptions include: (1) polar pit gullies at 68° S, where Raack et al. (2015) noted that the recent dark flows occurred in the spring, when the surface is still covered with CO$_2$ ice; (2) activity in large apron gullies on sand dunes between 40° S and 60° S, which occur in winter, when CO$_2$ frost is still present (Diniega et al. 2010; Pasquon et al., this volume, in review); and (3) mass wasting events on north polar dunes, that are active in the mid-winter, under the CO$_2$ ice slab (which although not strictly gullies, could represent processes active in gullies; Diniega et al. 2017). These three exceptions represent a small proportion of known active gullies. The remaining active gully sites comprise 'classic', mid-latitude gullies and linear dune gullies (Auld & Dixon 2016; Conway et al. 2017). As reported in Vincendon (2015) and Dundas et al. (2017), activity in mid-latitude classic gullies is limited to periods when thin (microns to centimetres) and patchy CO$_2$ or H$_2$O frost is present during, or just prior to the noted activity. So far, c. 67 such sites have been catalogued as active (Dundas et al. 2017), which is c. 18% of monitored sites in the southern hemisphere, but activity is sporadic, rather than annual. As reported in Reiss & Jaumann (2003), Reiss et al. (2010), Pasquon et al. (2016; this volume, in review and Jouannic et al. (this volume, in review), activity in linear dune gullies happens when the last CO$_2$ ice is disappearing from the pole-facing crest of the dune. Linear dune gullies are particularly active, with most of the 33 sites showing annual changes. Hence, in terms of timing and frost observations for both active 'classic' gullies and active linear gullies, the mechanism we have observed in the laboratory could be at work.

We re-emphasize here that our experiments cannot tell us what role sublimation of subsurface CO$_2$ frost is playing in forming the morphologies of these gully types, and we note that it may only be a secondary process (see further discussion on this point below). However, we think it should be considered among the candidates for morphological changes in these gullies for the following reasons. The substrate type is better known for linear dune gullies than for classic gullies. Sand dunes on Mars have been investigated in situ by rovers, the most recent study revealing grains ranging between 50 and 350 μm with a mean size of 113 μm (Ewing et al. 2017). Activity in linear gullies is only found where the crest of the dune is at 20° or higher, but the changes themselves occur on slopes down to 5–10° (Pasquon et al. 2016; Jouannic et al., this volume, in review). Both the substrate type and slope angles used in our experiments are consistent with these data, hence our results would predict movement in this context if CO$_2$ is condensed in to the subsurface. For classic gullies, we must rely on

orbital observations, with thermal inertia measurements suggesting that gullies reside in materials classed as unconsolidated 'sand- to pebble-sized grains' (Reiss et al. 2009; Harrison et al. 2014). Source areas for recent motions in classic gullies are usually diffuse, suggesting remobilization of a loose surface cover (Dundas et al. 2017) and source areas of classic gullies range upwards from 20° (median 25°; Conway et al. 2015). Results from our laboratory work and application of our analytical model reveal that these grain sizes and slope angles should be able to sustain the CO$_2$ sublimation-triggered failures that we have investigated in our experiments.

The range of sediments that could be mobilized on Mars could be wider than that encompassed by the fine sand and JSC Mars1 sediments used in our laboratory work. Our results indicate that the fine component of the sediment plays an important role in triggering activity at angles lower than the angle of repose. On Mars, dust (generally accepted as grains with >30 μm diameter) is abundant on the surface and in the atmosphere (e.g. Christensen 1986; Tomasko et al. 1999). However, further experiments would be required to assess how important this factor might be in triggering movement.

We also consider it possible that the mechanism of CO$_2$ sublimation-triggered failures we observed in the laboratory could also have occurred under climate conditions different from those observed on Mars today, which may explain some of the sediment transport that has contributed to gully formation on timescales of millions of years (Reiss et al. 2004; Schon et al. 2009; de Haas et al. 2015a). However, further modelling work to understand the plausible temporal and spatial extent of this process at the present day would be needed in order to confidently extrapolate this process into the past, an endeavour beyond the scope of this present work.

Our experiments investigated the triggering of failures of unconsolidated materials, and we observed two models of subsequent transport, granular flow and creep. A subtype of recent gully activity termed 'bright flows' has been found to have a morphology consistent with a classic granular flow (Pelletier et al. 2008; Kolb et al. 2010). However, other features of recent (and past) activity, including the transport of metre-scale boulders, the formation of levees and lobate termini (e.g. Dundas et al. 2010, 2014, 2017; Johnsson et al. 2014; de Haas et al. 2015b) require some viscosity or fluidization of the flow beyond that of a simple granular flow. Further, in linear gullies the new morphologies are complex, encompassing albedo changes, formation of pits, channels with levees and complex distributary networks on relatively low slopes (Diniega et al. 2013; Pasquon et al. 2016; this volume,

in review; McKeown *et al.* 2017; Jouannic *et al.*, this volume, in review). As discussed by Stewart & Nimmo (2002), CO_2 gas should dissipate too quickly to enable durable fluidization of a sublimation-triggered flow. However, the fluidization of CO_2 sublimation-triggered granular flows has not yet been studied in the laboratory and should therefore be a focus of future work in order to substantiate these calculations. Our observations that CO_2 sublimation can generate a creep-like movement in unconsolidated sediments is of particular relevance to Mars, because it could provide an explanation for lobate features (Gallagher & Balme 2011; Gallagher *et al.* 2011; Johnsson *et al.* 2012; Balme *et al.* 2013; Soare *et al.* 2016), which are often associated with Martian gullies. The closest terrestrial analogue for these features is solifluction lobes, which are uniquely associated with creep generated by freeze–thaw cycling of water in the ground, so our results provide a possible alternative that needs to be explored further.

Our laboratory work results only pertain to sediment transport of unconsolidated materials. The present-day observations of activity in classic gullies seem to only encompass the transport of unconsolidated sediments, as outlined above. However, these landforms, which have been dated to millions of years (Reiss *et al.* 2004; Schon *et al.* 2009; Johnsson *et al.* 2014), are incised into consolidated materials including both the ice-rich Latitude Dependent Mantle and bedrock (e.g. Dickson *et al.* 2015; de Haas *et al.* 2017). Erosion of the unconsolidated sublimation lag believed to be on top of the LDM should engender loss of the interstitial ice by sublimation, rendering further sediment available for transport (e.g. Pilorget & Forget 2016). However, for gully alcoves cut into bedrock, it remains an open question as to how material is weathered to render it transportable. It should be acknowledged that whether this is a primary feature of the gully-forming process is under debate (cf. de Haas *et al.* 2015*a*; Dickson *et al.* 2015). The relationship between this weathering and the action of CO_2 condensation–sublimation cycles is an area for future work.

Conclusions

We have experimentally investigated the effect of sublimating CO_2 on the downslope mass wasting of sediment under Martian atmospheric conditions. We tested three substrate types, fine sand (mean diameter 168 μm), coarse sand (mean diameter 594 μm) and a Mars regolith simulant (JSC Mars-1) over slope angles ranging from 10° to near the angle of repose, adding to the work of Sylvest *et al.* (2016), which only considered JSC Mars-1 near the angle of repose. We observed four principal

movement types: discrete flows, creep, gas entrainment and grain tumbling. Of these, creep and grain tumbling were not reported in Sylvest *et al.* (2016). The observed sediment movement types were influenced both by initial slope angle and by the nature of the regolith.

We found that significant volumes of sediment were only transported by the discrete flows and creep movements. In fine sand, these processes were only active at slope angles near the angle of repose and the volumes transported were of the same order as those transported in experiments using JSC Mars-1 at the angle of repose (82 cm^3 mean erosion for a surface area of 473 cm^2). For JSC Mars-1, these processes continued to transport equivalent volumes of sediment down to 20°, slightly less at 17° and negligible amounts at slope angles <17°. In our previous work we hypothesized that mass wasting was triggered by a lowering of the static friction angle by gas escaping through the substrate from sublimation. We tested this hypothesis by constructing an analytical model describing the physics of this process and found that when applied to our experimental parameters this model successfully predicts the activity observed in our experiments. With this validated model, we were able to predict that, under Martian gravity for equivalent sediment types, mass wasting could be triggered at even lower slope angles (movement should be possible for coarse sand near angle of repose, 25° for fine sand and on any slope for JSC Mars-1). This model also reveals that the reduction in permeability in the JSC Mars-1 owing to the presence of fines could be the key parameter for explaining this substrate's enhanced activity range compared with the two sands. Our results suggest that the absolute amount of CO_2 in the subsurface may control the amount of sediment moved. Further the vertical temperature profiles from our experiments reveal that CO_2 ice emplacement in the subsurface, in terms of vertical distribution and density, is a key parameter to elucidate in order to better understand the limits of sediment transport by CO_2 sublimation.

On Mars, we find that the CO_2 sublimation-triggered mass movements observed in our experiments could be applicable for explaining some of the movements seen in present-day mid-latitude gullies and linear dune gullies. Specifically, our experiments and analytical model reveal that the grain sizes and slopes should be compatible with this type of motion. Some of the features, including movements of metre-scale boulders, levees and lobate termini, are features that would require further experimentation to determine if CO_2 sublimation can explain them. Finally, we present the first observations of a creep-like motion caused by CO_2 sublimation and this could provide a viable alternative to water–ice

freeze–thaw cycles to explain the origin of lobate features often found in association with Martian gullies.

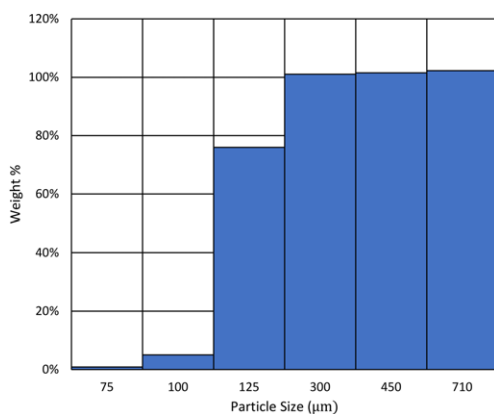# Appendix A

Method details

Fig. A1. Grain size distribution for fine sand.
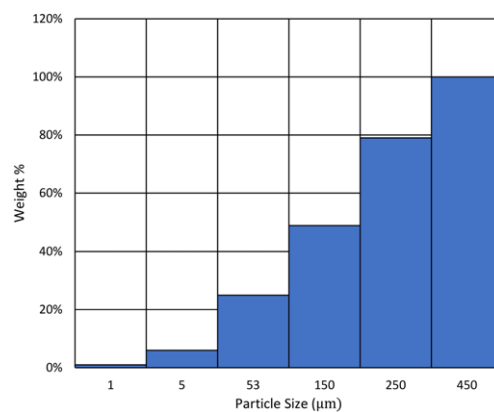
Fig. A3. Grain size distribution for JSC Mars-1.
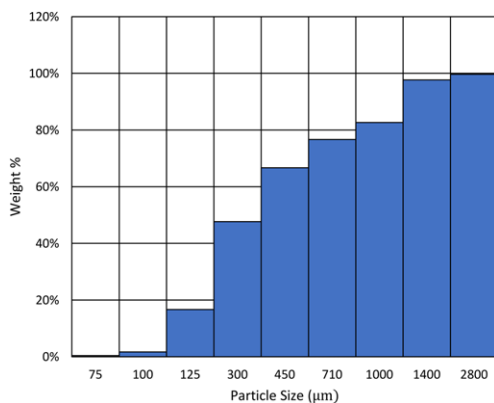
Fig. A2. Grain size distribution for coarse sand.

Table A1. *Summary of experimental parameters*

Parameter	Value
Heat lamp wattage	500 W
Maximum insolation intensity*	350 W m^{-2}
Chamber pressure at start of cooling	350 mbar
Maximum surface temperature at start of condensation	−120°C
Target chamber pressure during sublimation	5–7 mbar

*The heat transfer analysis used to estimate the maximum insolation intensity is presented in the Supporting Information from Sylvest et al. (2016).

Table A2. *Slope temperatures during the sublimation process*

Run ID	Sediment	Initial angle	Initial slope temperature (°C)			Final slope temperature (°C)		
			Surface	Mean	Basal	Surface	Mean	Basal
1	Fine sand	10°	−120.3	−132.2	−156.3	−31.3	−62.5	−93.9
2	Fine sand	15°	−118.3	−124.7	−137.3	12.7	10.6	11.1
3	Fine sand	20°	−133.1	−142.9	−163.5	−30.9	−59.2	−87.7
4	Fine sand	25°	−123.7	−139.9	−160.7	−38.7	−64.1	−85.4
5	Fine sand	25°	−128.4	−141.0	−160.6	−40.3	−64.8	−96.7
6	Fine sand	AOR	−127.0	−135.7	−150.2	−108.7	−116.9	−117.8
7	Fine sand	AOR	−121.5	−131.9	−169.6	−48.7	−73.4	−83.0
8	Fine sand	AOR	−122.6	−138.0	−165.3	−84.2	−99.0	−102.9
9	JSC Mars-1	10°	−135.0	−141.2	−169.2	−25.3	−50.6	−99.3
10	JSC Mars-1	15°	−133.8	−139.4	−167.5	−13.6	−47.2	−99.9
11	JSC Mars-1	15°	−134.6	−142.1	−167.9	−24.8	−50.5	−90.0
12	JSC Mars-1	15°	−132.4	−142.6	−167.6	−21.4	−51.4	−99.5
13	JSC Mars-1	17.5°	−127.3	−140.9	−167.3	−0.6	−44.9	−90.0
14	JSC Mars-1	17.5°	−128.5	−140.9	−167.4	−7.0	−45.6	−93.8
15	JSC Mars-1	17.5°	−122.4	−136.4	−161.6	−11.1	−44.5	−89.3
16	JSC Mars-1	17.5°	−128.6	−141.1	−165.4	−20.4	−45.1	−70.3
17	JSC Mars-1	20°	−133.1	−140.0	−167.0	−18.6	−51.1	−48.5
18	JSC Mars-1	20°	−127.6	−141.6	−166.7	−64.0	−89.4	−101.3
19	JSC Mars-1	20°	−124.4	−138.6	−144.5	−44.3	−79.8	−51.6
20	JSC Mars-1	AOR	−121.1	−128.6	−161.8	−52.6	−76.7	−109.6
21	JSC Mars-1	AOR	−120.3	−143.5	−171.2	−25.7	−61.8	−76.1
22	JSC Mars-1	AOR	−119.9	−143.4	−162.2	−34.9	−86.7	−109.6
23	JSC Mars-1	AOR	−123.3	−143.6	−167.1	−37.8	−76.3	−91.6
24	JSC Mars-1	AOR	−122.1	−120.7	−80.2	−36.8	−55.8	−33.4
25	Coarse sand	AOR	−124.9	−135.8	−150.2	13.4	12.1	14.3
26	Coarse sand	AOR	−112.2	−127.9	−143.6	−43.0	−77.2	−98.6

Photogrammetric methods details

Table A3. *Potential sources of error*

Error source	Comments
Noise in the captured video frames	
Lens distortion	The camera alignment procedure in PhotoScan determines internal camera parameters through self-calibration, which can be less effective than a laboratory-type camera calibration. A virtual set of camera locations with convergent geometry was employed to minimize this error.
Scanning distortion	Although a high frame rate was used (60 fps progressively scanned), this type of rolling shutter means very rapid movements can be offset from one edge of the charge coupled device (image sensor) to the other.
Poor placement of the cameras	Particularly important with only two cameras. The spacing and angles of the cameras relative to the slope surface can influence the accuracy of the resulting 3D measurements.
Errors in the physical measurement of the photogrammetric markers	The measurements are within <1 mm.
Errors in the placement of the photogrammetric reference markers in each of the captured video frames	Placements are within <1 mm.
Differences in lighting	
Differences in surface texture	

Table A4. *Photogrammetric error estimates*

Run ID	X rms (mm)	Y rms (mm)	Z rms (mm)	V_{noise} (cm^3)	$\%V_{noise}$ (cm^3)
1	1.00	0.94	0.57	4.20	0.12
2	1.01	1.52	0.47	6.01	0.18
3	1.27	1.35	0.82	24.85	0.79
4	1.35	1.25	0.64	14.37	0.53
5	1.38	1.75	0.54	10.45	0.30
6	1.00	0.84	1.32	58.75	1.73
7	1.69	1.60	0.59	11.34	0.37
8	1.66	2.69	2.29	100.89	2.91
9	2.02	2.68	0.58	13.68	0.41
10	1.00	1.04	0.54	31.19	0.75
11	1.02	0.93	0.57	15.18	0.35
12	0.98	0.89	1.00	42.50	1.10
13	1.64	2.42	0.83	34.11	0.86
14	1.05	0.94	0.69	20.67	0.56
15	1.00	0.93	0.43	3.02	0.07
16	2.52	3.06	0.72	4.70	0.12
17	0.96	8.87	0.70	23.27	0.67
18	0.99	0.97	0.71	24.43	1.06
19	1.03	1.08	0.55	1.75	0.08
20	0.23	1.30	0.79	8.49	0.18
21	0.53	1.21	0.95	24.79	0.61
22	0.96	1.12	1.32	59.02	1.25
23	4.37	0.69	1.37	49.88	1.71
24	0.59	0.60	0.55	1.18	0.03
25	n.d.	n.d.	n.d.	n.d.	n.d.
26	1.21	1.12	1.20	46.97	1.30

rms, root mean square error; n.d., no data. *X*, Long-slope coordinate; *Y*, cross-slope coordinate.

Results

Table A5. *Pearson correlation coefficients*

	Initial angle v. erosion	Initial angle v. deposition	Frost volume v. erosion	Frost volume v. deposition
JSC Mars-1	0.707	0.675	0.195	0.361
Fine sand	0.530	0.098	−0.378	0.065

Note: Correlation coefficients for coarse sand would be meaningless, as there were only two runs with this sediment.

Appendix B

Physical model

The system of equations (4 and 5) does not have a similarity solution in simple functions, but approximate solutions can be generated by a variety of methods. For long times, most of the heat has gone into heating the sand, and only a smaller fraction into subliming CO$_2$. In this regime $X(t) \propto \sqrt{t}$. For short times, however, most of the heat goes into subliming CO$_2$, and $X(t) \propto t$. A simple method to get an approximate solution is to assume an approximate temperature profile of the form

$$T(t,x) = \begin{cases} T_s + \left(1 - \dfrac{x}{X(t)}\right)\left(T_1(t) + T_2(t)\dfrac{x}{X(t)}\right), \\ T_s \end{cases}$$
$$x \in [0, X(t)] \quad 0 \le x \le X(t)$$
$$x > X(t) \tag{B1}$$

This is similar to the approach of Goodman (1958). All three boundary conditions are satisfied if

$$T_1 = X\frac{\rho_i e \dot{X} + Q}{2\kappa} \tag{B2}$$

Table B1. *Model parameters for internal friction angle calculations*

Symbol	Value			Definition
Q	350 W m^{-2}			Radiant heating
p_0	510 Pa			Atmospheric pressure
g	9.81 m s^{-2}			Terrestrial gravity
g_M	3.71 m s^{-2}			Martian gravity
e	5.7×10^5 J kg^{-1}			Enthalpy of sublimation for CO_2
ν	1.3×10^{-5} Pa s			Dynamic viscosity of CO_2
ρ_g	5×10^{-2} kg m^{-3}			Gas density of CO_2
ρ_i	15 kg m^{-3}			Solid density of interpore CO_2 frost
μ	tan 30°			Bed friction‡
	Fine sand	JSC Mars-1	Coarse sand	
κ	0.2 W m K^{-1}	0.08 W m K^{-1}*	0.2 W m K^{-1}	Thermal conductivity
c	680 J kg^{-1} K^{-1}	448 J kg^{-1} K^{-1}†	680 J kg^{-1} K^{-1}	Heat capacity
ρ_s	1.68×10^3 kg m^{-3}	0.871×10^3 kg m^{-3}	1.70×10^3 kg m^{-3}	Bulk density
k	1.51×10^{-10} m^2	3.0×10^{-11} m^2	5.99×10^{-10} m^{-2}	Permeability

*Seiferlin *et al.* (2008).
†Siegler *et al.* (2012).
‡Where 30° is the assumed initial internal friction angle.

$$T_2 = X \frac{\rho_i e \dot{X} - Q}{2\kappa} \quad \text{(B3)}$$

The final equation comes from requiring that the mean error in the conduction equation is zero, or that the total heat input matches the sublimation energy and heat increase in the sand. That is

$$Qt = \rho_i eX + \int_0^X \rho_s c(T - T_s)\, dx \quad \text{(B4)}$$

This equation simplifies to an ODE in $f(s)$

$$f^2 f' + \frac{f^2}{2} + 3f = 3s \quad \text{(B5)}$$

This equation cannot be solved exactly. It is like an Abel equation, but with a quartic, rather than a cubic, form. It can easily be solved numerically, or approximated numerically. We are primarily concerned with the derivative, f', since this sets the gas flux. This is well approximated by

$$f' = \frac{1 + 3s/5}{\sqrt{1 + 3s + 2s^2 + s^3/25}} \quad \text{(B6)}$$

and has the exact large and small s behaviour. The flux rate falls to half its initial value when $s \approx 2.5$. With the numbers in Table B1 (Mars conditions), we get a 5.1° reduction of bed friction angle, θ, for fine sand and a 50.3° reduction for JSC Mars-1. The unphysically large reduction for JSC Mars-1 (greater than the angle of repose) implies that the sublimed CO_2 gas is capable of levitating grains of this regolith at any angle, which is consistent with the observed entrainment behaviour described above. The much smaller reduction of bed friction angle for fine sand is also consistent with our results, these slopes only failing at angles near the static angle of repose.

References

ALLEN, C.C., MORRIS, R.V., KAREN, M.J., GOLDEN, D.C., LINDSTROM, M.M. & LOCKWOOD, J.P. 1998. Martian Regolith Simulant JSC Mars-1. *Lunar and Planetary Science Conference XXVIII*, 1690.

APPÉRÉ, T., SCHMITT, B. ET AL. 2011. Winter and spring evolution of northern seasonal deposits on Mars from OMEGA on Mars Express. *Journal of Geophysical Research E Planets*, **116**, https://doi.org/10.1029/2010JE003762

AULD, K.S. & DIXON, J.C. 2016. A classification of Martian gullies from HiRISE imagery. *Planetary and Space Science*, **131**, 88–101, https://doi.org/10.1016/j.pss.2016.08.002

BALME, M.R., GALLAGHER, C.J. & HAUBER, E. 2013. Morphological evidence for geologically young thaw of ice on Mars: a review of recent studies using high-resolution imaging data. *Progress in Physical Geography*, **37**, 289–324, https://doi.org/10.1177/0309133313477123

BARGERY, A.S., BALME, M.R., WARNER, N., GALLAGHER, C.J. & GUPTA, S. 2011. A background to Mars exploration and research. *In*: BALME, M.R., BARGERY, A.S., GALLAGHER, C.J. & GUPTA, S. (eds) *Martian Geomorphology*. Geological Society, London, Special Publications, **356**, 5–20, https://doi.org/10.1144/SP356.2

CEDILLO-FLORES, Y., TREIMAN, A.H., LASUE, J. & CLIFFORD, S.M. 2011. CO_2 gas fluidization in the initiation and formation of Martian polar gullies. *Geophysical Research Letters*, **38**, https://doi.org/10.1029/2011GL049403

CHRISTENSEN, P.R. 1986. Regional dust deposits on Mars: physical properties, age, and history. *Journal of Geophysical Research*, **91**, 3533–3545, https://doi.org/10.1029/JB091iB03p03533

COLEMAN, K.A., DIXON, J.C., HOWE, K.L., ROE, L.A. & CHEVRIER, V. 2009. Experimental simulation of Martian gully forms. *Planetary and Space Science*, **57**, 711–716, https://doi.org/10.1016/j.pss.2008.11.002

CONWAY, S.J., LAMB, M.P., BALME, M.R., TOWNER, M.C. & MURRAY, J.B. 2011a. Enhanced runout and erosion by overland flow at low pressure and sub-freezing conditions: experiments and application to Mars. *Icarus*, **211**, 443–457, https://doi.org/10.1016/j.icarus.2010.08.026

CONWAY, S.J., BALME, M.R., MURRAY, J.B., TOWNER, M.C., OKUBO, C.H. & GRINDROD, P.M. 2011b. The indication of Martian gully formation processes by slope-area analysis. *In*: BALME, M.R., BARGERY, A.S., GALLAGHER, C.J. & GUPTA, S. (eds) *Martian Geomorphology*. Geological Society, London, Special Publications, **356**, 171–201, https://doi.org/10.1144/SP356.10

CONWAY, S.J., BALME, M.R., KRESLAVSKY, M.A., MURRAY, J.B. & TOWNER, M.C. 2015. The comparison of topographic long profiles of gullies on Earth to gullies on Mars: a signal of water on Mars. *Icarus*, **253**, 189–204, https://doi.org/10.1016/j.icarus.2015.03.009

CONWAY, S.J., HARRISON, T.N., SOARE, R.J., BRITTON, A.W. & STEELE, L.J. 2017. New slope-normalized global gully density and orientation maps for Mars. *In*: CONWAY, S.J., CARRIVICK, J.L., CARLING, P.A., DE HAAS, T. & HARRISON, T.N. (eds) *Martian Gullies and their Earth Analogues*. Geological Society, London, Special Publications, **467**. First published online November 27, 2017, https://doi.org/10.1144/SP467.3

DE HAAS, T., CONWAY, S.J. & KRAUTBLATTER, M. 2015a. Recent (Late Amazonian) enhanced backweathering rates on Mars: paracratering evidence from gully alcoves. *Journal of Geophysical Research E Planets*, **120**, 2169–2189, https://doi.org/10.1002/2015JE004915

DE HAAS, T., VENTRA, D., HAUBER, E., CONWAY, S.J. & KLEINHANS, M.G. 2015b. Sedimentological analyses of Martian gullies: The subsurface as the key to the surface. *Icarus*, **258**, 92–108, https://doi.org/10.1016/j.icarus.2015.06.017

DE HAAS, T., CONWAY, S.J., BUTCHER, F.E.G., LEVY, J., GRINDROD, P.M., GOUDGE, T.A. & BALME, M.R. 2017. Time will tell: temporal evolution of Martian gullies and paleoclimatic implications. *In*: CONWAY, S.J., CARRIVICK, J.L., CARLING, P.A., DE HAAS, T. & HARRISON, T.N. (eds) *Martian Gullies and Their Earth Analogues*. Geological Society, London, Special Publications, **467**. First published online November 27, 2017, https://doi.org/10.1144/SP467.1

DICKSON, J.L., HEAD, J.W. & KRESLAVSKY, M. 2007. Martian gullies in the southern mid-latitudes of Mars: evidence for climate-controlled formation of young fluvial features based upon local and global topography. *Icarus*, **188**, 315–323, https://doi.org/10.1016/j.icarus.2006.11.020

DICKSON, J.L., HEAD, J.W., GOUDGE, T.A. & BARBIERI, L. 2015. Recent climate cycles on Mars: stratigraphic relationships between multiple generations of gullies and the latitude dependent mantle. *Icarus*, **252**, 83–94, https://doi.org/10.1016/j.icarus.2014.12.035

DINIEGA, S., BYRNE, S., BRIDGES, N.T., DUNDAS, C.M. & MCEWEN, A.S. 2010. Seasonality of present-day Martian dune-gully activity. *Geology*, **38**, 1047–1050, https://doi.org/10.1130/G31287.1

DINIEGA, S., HANSEN, C.J., MCELWAINE, J.N., HUGENHOLTZ, C.H., DUNDAS, C.M., MCEWEN, A.S. & BOURKE, M.C. 2013. A new dry hypothesis for the formation of Martian linear gullies. *Icarus*, **225**, 526–537, https://doi.org/10.1016/j.icarus.2013.04.006

DINIEGA, S., HANSEN, C.J., ALLEN, A., GRIGSBY, N., LI, Z., PEREZ, T. & CHOJNACKI, M. 2017. Dune-slope activity due to frost and wind throughout the north polar erg, Mars. *In*: CONWAY, S.J., CARRIVICK, J.L., CARLING, P.A., DE HAAS, T. & HARRISON, T.N. (eds) *Martian Gullies and their Earth Analogues*. Geological Society, London, Special Publications, **467**. First published online November 27, 2017, https://doi.org/10.1144/SP467.6

DUNDAS, C.M., MCEWEN, A.S., DINIEGA, S., BYRNE, S. & MARTINEZ-ALONSO, S. 2010. New and recent gully activity on Mars as seen by HiRISE. *Geophysical Research Letters*, **37**, https://doi.org/10.1029/2009GL041351

DUNDAS, C.M., DINIEGA, S., HANSEN, C.J., BYRNE, S. & MCEWEN, A.S. 2012. Seasonal activity and morphological changes in Martian gullies. *Icarus*, **220**, 124–143, https://doi.org/10.1016/j.icarus.2012.04.005

DUNDAS, C.M., DINIEGA, S. & MCEWEN, A.S. 2014. Long-term monitoring of Martian gully activity with HiRISE. Abstract 2204, presented at the 45th Lunar Planetary Science Conference, 86001.

DUNDAS, C.M., MCEWEN, A.S., DINIEGA, S., HANSEN, C.J., BYRNE, S. & MCELWAINE, J.N. 2017. The formation of Gullies on Mars today. *In*: CONWAY, S.J., CARRIVICK, J.L., CARLING, P.A., DE HAAS, T. & HARRISON, T.N. (eds) *Martian Gullies and their Earth Analogues*. Geological Society, London, Special Publications, **467**. First published online November 27, 2017, https://doi.org/10.1144/SP467.5

EWING, R.C., LAPOTRE, M.G.A. *ET AL.* 2017. Sedimentary processes of the Bagnold Dunes: implications for the eolian rock record of Mars. *Journal of Geophysical Research Planets*, https://doi.org/10.1002/2017JE005324

GALLAGHER, C.J. & BALME, M.R. 2011. Landforms indicative of ground-ice thaw in the northern high latitudes of Mars. *In*: BALME, M.R., BARGERY, A.S., GALLAGHER, C.J. & GUPTA, S. (eds) *Martian Geomorphology*. Geological Society, London, Special Publications, **356**, 87–110, https://doi.org/10.1144/SP356.6

GALLAGHER, C., BALME, M.R., CONWAY, S.J. & GRINDROD, P.M. 2011. Sorted clastic stripes, lobes and associated gullies in high-latitude craters on Mars: landforms indicative of very recent, polycyclic ground-ice thaw and liquid flows. *Icarus*, **211**, 458–471, https://doi.org/10.1016/j.icarus.2010.09.010

GARDIN, E., ALLEMAND, P., QUANTIN, C. & THOLLOT, P. 2010. Defrosting, dark flow features, and dune activity on Mars: example in Russell crater. *Journal of Geophysical Research*, **115**, E06016, https://doi.org/10.1029/2009JE003515

GOODMAN, T.R. 1958. The heat-balance integral and its application to problems involving a change of phase. *Transactions of the ASME Journal*, **80**, 335–342.

HAGERMANN, A. 2005. Planetary heat flow measurements. *Philosophical Transactions of the Royal Society: A. Mathematical, Physical and Engineering Science*, **363**, 2777–2791, https://doi.org/10.1098/rsta.2005.1664

HANSEN, C.J., BOURKE, M. *ET AL.* 2011. Seasonal erosion and restoration of Mars' Northern Polar Dunes. *Science*, **331**, 575–578, https://doi.org/10.1126/science.1197636

HARRISON, T.N., OSINSKI, G.R. & TORNABENE, L.L. 2014. Global documentation of Gullies with the Mars Reconnaissance Orbiter Context Camera (CTX) and implications for their formation. Abstract 2124, presented at the 45th Lunar Planetary Science Conference, https://doi.org/10.1016/j.icarus.2015.01.022

HESS, S.L., HENRY, R.M. & TILLMAN, J.E. 1979. The seasonal variation of atmospheric pressure on Mars as affected by the south polar cap. *Journal of Geophysical Research*, **84**, 2923–2927, https://doi.org/10.1029/JB084iB06p02923

HESS, S.L., RYAN, J.A., TILLMAN, J.E., HENRY, R.M. & LEOVY, C.B. 1980. The annual cycle of pressure on Mars measured by Viking Landers 1 and 2. *Geophysical Research Letters*, **7**, 197–200, https://doi.org/10.1029/GL007i003p00197

JOHNSSON, A., REISS, D., HAUBER, E., ZANETTI, M., HIESINGER, H., JOHANSSON, L. & OLVMO, M. 2012. Periglacial mass-wasting landforms on Mars suggestive of transient liquid water in the recent past: insights from solifluction lobes on Svalbard. *Icarus*, **218**, 489–505, https://doi.org/10.1016/j.icarus.2011.12.021

JOHNSSON, A., REISS, D., HAUBER, E., HIESINGER, H. & ZANETTI, M. 2014. Evidence for very recent melt-water and debris flow activity in gullies in a young mid-latitude crater on Mars. *Icarus*, **235**, 37–54, https://doi.org/10.1016/j.icarus.2014.03.005

JOUANNIC, G., GARGANI, J. *ET AL.* 2015. Laboratory simulation of debris flows over sand dunes: insights into gully-formation (Mars). *Geomorphology*, **231**, 101–115, https://doi.org/10.1016/j.geomorph.2014.12.007

JOUANNIC, G., GARGANI, J. *ET AL.* In review. Morphological characterization of landforms produced by springtime seasonal activity on Russell dune (Mars). *In*: CONWAY, S.J., CARRIVICK, J.L., CARLING, P.A., DE HAAS, T. & HARRISON, T.N. (eds) *Martian Gullies and Their Earth Analogues*. Geological Society, London, Special Publications, **467**.

KOLB, K.J., PELLETIER, J.D. & MCEWEN, A.S. 2010. Modeling the formation of bright slope deposits associated with gullies in Hale Crater, Mars: implications for recent liquid water. *Icarus*, **205**, 113–137, https://doi.org/10.1016/j.icarus.2009.09.009

MALIN, M.C. & EDGETT, K.S. 2000. Evidence for recent groundwater seepage and surface runoff on Mars. *Science*, **288**, 2330–2335, https://doi.org/10.1126/science.288.5475.2330

MCEWEN, A.S., OJHA, L. *ET AL.* 2011. Seasonal flows on warm Martian slopes. *Science*, **333**, 740–743, https://doi.org/10.1126/science.1204816

MCGLYNN, I.O., FEDO, C.M. & MCSWEEN, H.Y. 2011. Origin of basaltic soils at Gusev crater, Mars, by aeolian modification of impact-generated sediment. *Journal of Geophysical Research*, **116**, E00F22, https://doi.org/10.1029/2010JE003712

MCKEOWN, L.E., BOURKE, M.C. & MCELWAINE, J.N. 2017. Experiments on sublimating carbon dioxide ice and implications for contemporary surface processes on Mars. *Science Reports*, **7**, 14181, https://doi.org/10.1038/s41598-017-14132-2

MELLON, M.T.M.T., JAKOSY, B.M. & JAKOSKY, B.M. 1993. Geographic variations in the thermal and diffusive stability of ground ice on Mars. *Journal of Geophysical Research*, **98**, 3345–3364, https://doi.org/10.1029/92JE02355

PASQUON, K., GARGANI, J., MASSÉ, M. & CONWAY, S.J. 2016. Present-day formation and seasonal evolution of linear dune gullies on Mars. *Icarus*, **274**, 195–210, https://doi.org/10.1016/j.icarus.2016.03.024

PASQUON, K., GARGANI, J. *ET AL.* In review. Are the different gully morphologies due to different formation processes on the Kaiser dune field? *In*: CONWAY, S.J., CARRIVICK, J.L., CARLING, P.A., DE HAAS, T. & HARRISON, T.N. (eds) *Martian Gullies and their Earth Analogues*. Geological Society, London, Special Publications, **467**.

PELLETIER, J.D., KOLB, K.J., MCEWEN, A.S. & KIRK, R.L. 2008. Recent bright gully deposits on Mars: wet or dry flow? *Geology*, **36**, 211–214, https://doi.org/10.1130/G24346A.1

PILORGET, C. & FORGET, F. 2016. Formation of gullies on Mars by debris flows triggered by CO_2 sublimation. *Nature Geosciences*, **9**, 65–69, https://doi.org/10.1038/ngeo2619

PIQUEUX, S., KLEINBÖHL, A., HAYNE, P.O., KASS, D.M., SCHOFIELD, J.T. & MCCLEESE, D.J. 2015. Variability of the Martian seasonal CO_2 cap extent over eight Mars Years. *Icarus*, **251**, 164–180, https://doi.org/10.1016/j.icarus.2014.10.045

RAACK, J., REISS, D., APPÉRÉ, T., VINCENDON, M., RUESCH, O. & HIESINGER, H. 2015. Present-day seasonal gully activity in a south polar pit (Sisyphi Cavi) on Mars. *Icarus*, **251**, 226–243, https://doi.org/10.1016/j.icarus.2014.03.040

RAACK, J., CONWAY, S.J., HERNY, C., BALME, M.R., CARPY, S. & PATEL, M.R. 2017. Water-induced sediment levitation enhances downslope transport on Mars. *Nature Communications*, **8**, https://doi.org/10.1038/s41467-017-01213-z

REISS, D. & JAUMANN, R. 2003. Recent debris flows on Mars: seasonal observations of the Russell Crater dune field. *Geophysical Research Letters*, **30**, 3–6, https://doi.org/10.1029/2002GL016704

REISS, D., VAN GASSELT, S., NEUKUM, G. & JAUMANN, R. 2004. Absolute dune ages and implications for the time of formation of gullies in Nirgal Vallis, Mars. *Journal of Geophysical Research E Planets*, **109**, 1–9, https://doi.org/10.1029/2004JE002251

REISS, D., HIESINGER, H., HAUBER, E. & GWINNER, K. 2009. Regional differences in gully occurrence on Mars: a comparison between the Hale and Bond craters. *Planetary and Space Science*, **57**, 958–974, https://doi.org/10.1016/j.pss.2008.09.008

REISS, D., ERKELING, G., BAUCH, K.E. & HIESINGER, H. 2010. Evidence for present day gully activity on the Russell crater dune field, Mars. *Geophysical Research Letters*, **37**, https://doi.org/10.1029/2009GL042192

SCHON, S.C., HEAD, J.W. & FASSETT, C.I. 2009. Unique chronostratigraphic marker in depositional fan stratigraphy on Mars: evidence for *c.* 1.25 Ma gully activity and surficial meltwater origin. *Geology*, **37**, 207–210, https://doi.org/10.1130/G25398A.1

SEIFERLIN, K., EHRENFREUND, P. *ET AL.* 2008. Simulating Martian regolith in the laboratory. *Planetary and Space Science*, **56**, 2009–2025, https://doi.org/10.1016/j.pss.2008.09.017

SIEGLER, M., AHARONSON, O., CAREY, E., CHOUKROUN, M., HUDSON, T., SCHORGHOFER, N. & XU, S. 2012. Measurements of thermal properties of icy Mars regolith analogs. *Journal of Geophysical Research E Planets*, **117**, 1–24, https://doi.org/10.1029/2011JE003938

SIZEMORE, H.G. & MELLON, M.T. 2008. Laboratory characterization of the structural properties controlling dynamical gas transport in Mars-analog soils. *Icarus*, **197**, 606–620, https://doi.org/10.1016/j.icarus.2008.05.013

SOARE, R.J., CONWAY, S.J., GALLAGHER, C. & DOHM, J.M. 2016. Sorted (clastic) polygons in the Argyre region, Mars, and possible evidence of pre- and post-glacial periglaciation in the Late Amazonian Epoch. *Icarus*, **264**, 184–197, https://doi.org/10.1016/j.icarus.2015.09.019

STEWART, S.T. & NIMMO, F. 2002. Surface runoff features on Mars: testing the carbon dioxide formation hypothesis. *Journal of Geophysical Research*, **107**, 5069, https://doi.org/10.1029/2000JE001465

SYLVEST, M.E., CONWAY, S.J., PATEL, M.R., DIXON, J.C. & BARNES, A. 2016. Mass wasting triggered by seasonal CO$_2$ sublimation under Martian atmospheric conditions: laboratory experiments. *Geophysical Research Letters*, **43**, 12363–12370, https://doi.org/10.1002/2016GL071022

TOMASKO, M.G., DOOSE, L.R., LEMMON, M., SMITH, P.H. & WEGRYN, E. 1999. Properties of dust in the Martian atmosphere from the Imager on Mars Pathfinder. *Journal of Geophysical Research*, **104**, 8987, https://doi.org/10.1029/1998JE900016

VINCENDON, M. 2015. Identification of Mars gully activity types associated with ice composition. *Journal of Geophysical Research E Planets*, **120**, 1859–1879, https://doi.org/10.1002/2015JE004909